MSc Thesis

Characterizing low-frequency flame-front oscillations – An investigation into their origin and possible mitigation

Aravind Krishna Madhavan

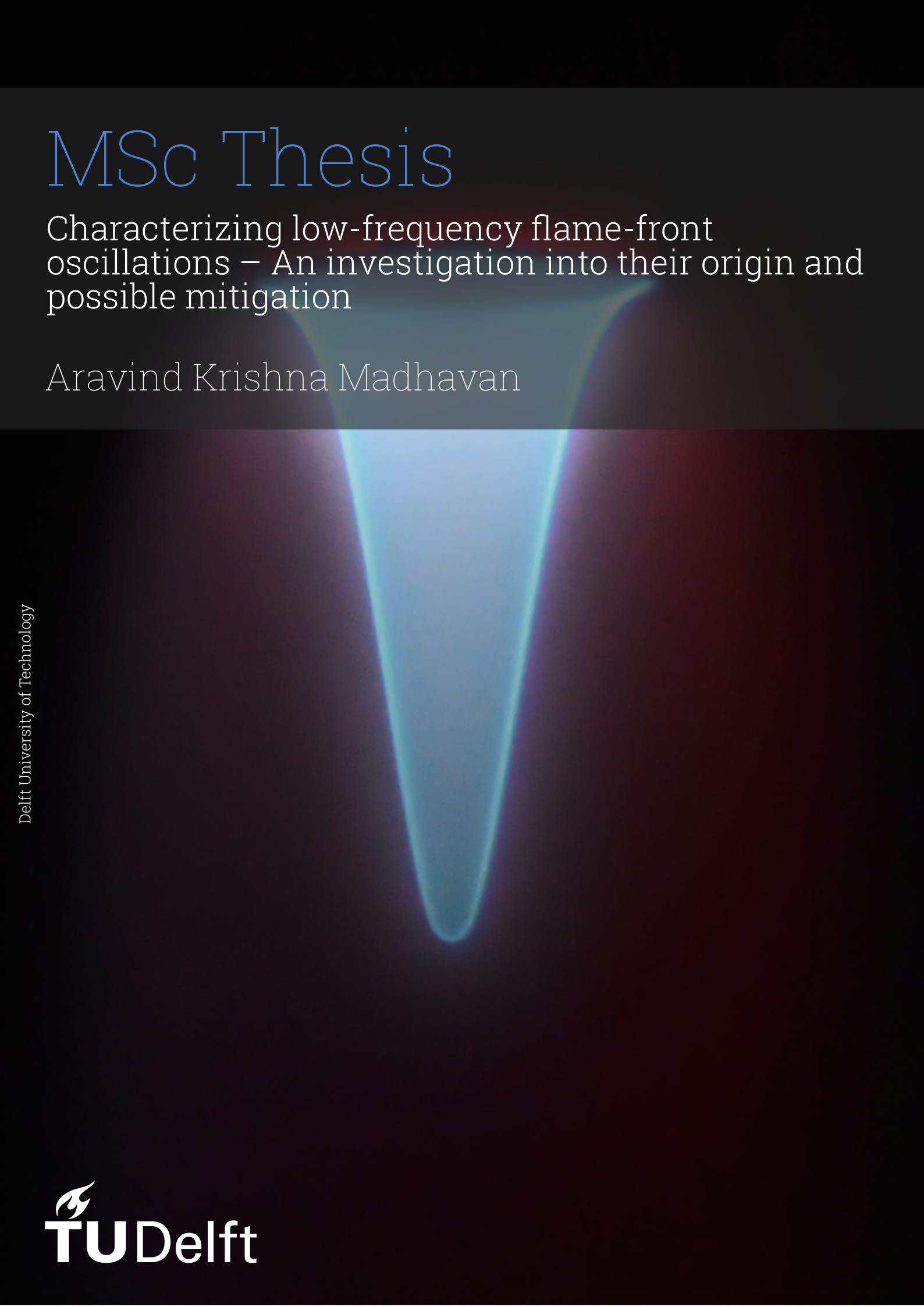

Delft University of Technology

TU Delft

MSc Thesis

Characterizing low-frequency flame-front oscillations – An investigation into their origin and possible mitigation

by

Aravind Krishna Madhavan

Supervisor:	Alexis Bohlin
Daily Supervisor:	Leonardo Castellanos
Project Duration:	July 2020 - December 2022
Faculty:	Faculty of Aerospace Engineering, Delft

Cover: Inverted conical flame on a laminar premixed burner (experiment photograph)

TU Delft

Preface

While the rapid pace of commercial aviation has led to the betterment of human civilization, the side effects of such progress have been relatively slow to catch up. Personally, a large part of my life has been made possible via these advancements. Beginning from the barely self-sustaining designs of Whittle to the geared turbofan engines of the present day, it is true that the efficiency of gas turbine engines has substantially increased. On the other hand, the focus of such progressive improvements has been primarily on the large-scale engineering components of this device such as the compressor and turbine assembly.

Driven by the overall appeal and admiration toward the field of aerospace engineering, my path from the undergraduate degree I chose to this current thesis topic has been extremely enriching. Along the way, theoretical concepts such as the basics of combustion, emissions, and diagnostic methods. By the time my academic courses were completed, I began searching for a thesis topic that would align with my interests. Naturally, topics related to the analysis of combustion and its instabilities became a focal point during this search. Following discussions with Dr. Alexis Bohlin, the details of the research direction in terms of its emphasis on hands-on experimentation were especially attractive to me. Specifically, the investigation of the origins of such low-frequency oscillations within conical flames was decided as the final topic. While the thesis focuses on the factors that affect the flame front, it merely employs various diagnostic techniques with varying levels of complexity. Following preliminary experimentation to generate reference data with existing lab setups, control experiments were successfully performed to isolate and test the various hypotheses for such oscillations. Through the guidance of my daily supervisor Leonardo Castellanos, the nuances of going about the process of configuring and planning experiments were greatly expedited. While the outcomes of this experiment are minuscule in comparison to the overall progress made in terms of combustion stability, I hope that it still acts as a step further toward the goal.

Aravind Krishna Madhavan
Delft, June 2023

Abstract

The premixed conical flame, a mainstay of combustion diagnostics is the focus of this investigation. While the properties of the canonical bunsen flame have been studied extensively, such endeavors have been aimed toward large-scale phenomena (high-frequency oscillations). This thesis aims to explain the origins of low-frequency oscillations that affect such flame fronts, concluding with suggestions for mitigating them based on their origin. Aimed towards improving high-accuracy diagnostics of standard conical flames, the generation of stable flame plumes via the reduction of such oscillations is an integral part of the solution. The central aim of this thesis report is to ascertain a solution among two possible theories for such low-frequency oscillations- buoyancy variations (phenomenon-based) and flow rate fluctuations (experiment based). The use of image chemiluminescence and CARS spectroscopy have been employed for ascertaining the validity of these hypotheses. Algorithms for detecting the flame front boundary have been implemented to discern spatial oscillations. Alternatively, the use of CARS analysis has been reserved for validating the presence of fluctuations indirectly. Preliminary experiments have been performed for generating reference data sets followed by the primary experimental campaign. Within the primary campaign, experiments have been tailored to span a range of Reynolds numbers from 500-1000 for constant equivalence ratios. This is being performed as a means of isolating the effect of buoyancy variations. In addition to the observations made regarding these two possibilities, the report concludes with details suggesting possible design changes for the flame holder to reduce the amplitude of the instabilities in question.

Contents

List of Figures

List of Tables

Nomenclature

If a nomenclature is required, a simple template can be found below for convenience. Feel free to use, adapt or completely remove.

Abbreviations

Abbreviation	Definition
CARS	Coherent Anti-Stokes Raman Spectroscopy
ICAO	International Civil Aviation Organization
PLIF	Planar Laser Induced Fluorescence
PIV	Particle Image Velocimetry
CMOS	Complementary metal–oxide–semiconductor
HPF	High pass filter
LPF	Low pass filter
SN	Signal to noise ratio
FFT	Fast Fourier transform
ESF	Edge spread function
LSF	Line spread function
FWHM	Full width half-maximum
SHBC	Second harmonic bandwidth compressor
HWP	Half wave plate
POL	Polarizer
VCL	Vertically aligned cylindrical lens
BPF	Bandpass filter
TS	Translation stage
SL	Spherical lens
TG	Transmission grating

Symbols

Symbol	Definition	Unit
Ri	Richardson number	
Re	Reynolds number	
St	Strouhal number	
$Stoch_{ratio}$	Stochiometric ratio	
$M.F_{fuel}$	Mass fraction of fuel	
$M.F_{oxid}$	Mass fraction of oxidizer	
n_{CH4}	Number of moles of fuel	$moles$
n_{N_2}	Number of moles of nitrogen	$moles$
n_{O_2}	Number of moles of oxygen	$moles$
n_{total}	Number of moles of oxidizer	$moles$
$F.A$	Ratio between quantities of fuel to oxidizer	
$F.A_{stoch}$	Stoch. ratio between quantities of fuel to oxidizer	
LPM	Litres per minute	l/min

Symbol	Definition	Unit
V_u	Flow velocity of premixed reactant mixture	m/s
$V_{unormal}$	Normal component of flow velocity of premixed reactant mixture	m/s
S_L	Laminar burning velocity	m/s
Q_r	Reactant flow rate	kg/s
u_r	Reactant flow velocity	m/s
D	Burner diameter	m
T_p	Temperature of the product gases	K
T_r	Temperature of the reactants	K
T_{adiab}	Temperature of the flame-front assuming adiabatic conditions	K
T_{amb}	Temperature of the ambient surroundings	K
B	Buoyancy term	
S	Shearing term	
z	Position with respect to the axis of the flame-front	m
g	Acceleration due to gravity	m/s^2
F_{co}	Correction factor (Constant of proportionality)	
u	Horizontal coordinates of the image/kernel matrix	
v	Vertical coordinates of the image/kernel matrix	
D_0	Cut-off frequency of the high/low pass filter	Hz
n	Order of the high/low pass filter	
ρ_r	Density of reactant mixture	kg/m^3
ρ_p	Density of product gases	kg/m^3
ϕ	Equivalence ratio	
μ	Oxidizer viscosity	Ns/m^2
τ	Heat release ratio	
ν	Oscillation frequency of the flame front	Hz
ν_f	Flow rate fluctuation frequency	Hz

1

Introduction

Since the advent of the gas turbine engine, the indirect effects of commercial aviation have burgeoned. As a consequence, a concerted effort toward the reduction of greenhouse emissions has been ongoing. It has become apparent in recent years that the targets set by organizations such as the ICAO (International Civil Aviation Organization) of a 2% annual fuel efficiency improvement have stayed extremely divergent from reality. If one were to survey the various solutions proposed to reduce the gap between expectations and real life are electric propulsion, alternate fuels (hydrogen, methane, etc.), and flame-less combustor designs. However, in all of the above solutions with a few exceptions, the core fundamentals of combustion still remain. This implies that research on improving the quality of the combustion process can still play an important part in the betterment of sustainable aviation. investigating methods to improve the stability of flames.

When speaking about the quality of combustion, it is evident that a fundamental understanding of the factors involved is clearly necessary. The conventional way to achieve this in any field would be to perform experimental observations, propose hypotheses and model the occurrences recorded. In the case of studies involving combustion, the characterization of standardized canonical flame fronts is the first step. While the ideal laboratory conditions under which such analysis is carried out do not mirror the reality of their commercial applications, it is important to understand the isolated behavior of these flames prior to their integration into more complex systems such as gas turbines, internal combustion engines, etc.

It is at this stage of the analysis that the existence of a widely observed phenomenon comes into the picture. Despite the extremely ideal conditions under which these conventional canonical flames are being tested, the occurrence of low-scale fluctuations is present without exception. Such oscillatory behavior while imperceptible to the naked eye plays a detrimental role in terms of the accuracy with which information regarding the properties of a flame front can be recorded. To demonstrate this fact, a review of the accuracy with which various diagnostic equipment has been used to determine the laminar burner velocity for a stochiometric methane-air flame has been charted by Ahmed et al [1]. While the review does not specifically account for the presence of such oscillatory behavior, the variation in the numerical values recorded even within contemporary evaluations suggests the severity of the problem. While technological improvements within diagnostic solutions may appear as the solution, the problem is rather counter-intuitive. With ever-increasing spatial resolution and temporal resolution, the detrimental effects of these low-scale flame front fluctuations have only increased. Consider for instance the standard conical flame front of a methane-air premixed flame. Assuming that the thickness of the flame front ranges in the order of 500-1000 microns [2], a high-fidelity system such as two-beam femtosecond CARS (Coherent Anti-Stokes Raman Spectroscopy) [3] is then employed such that its probe volume is placed within this flame front region. Under these circumstances, the observed low-frequency fluctuations between 40-80 microns in amplitude as reported by Castellanos et al [4] are substantially larger in size than the spatial resolution of the CARS setup at 20 microns [4]. In practical terms, this massive discrepancy between spatial resolution and the amplitude of the fluctuation will only worsen with improvements to diagnostic technology. As a result of this problem, thermometry readings

are only one instance of inaccurate measurements being generated by the presence of fluctuations.

This thesis attempts to address this problem by exploring the origins of these low-scale flame front oscillations in order to produce solutions to mitigate such fluctuations. Using an experimental approach, the conventional conical premixed flame has been used to test for trends associated with specific hypotheses. These hypotheses have been categorized into two main types. The first involves phenomenological factors of which buoyancy forces form the primary cause. For testing this hypothesis, a preexisting mathematical model is studied parametrically to verify the influence of the variables involved within it. The second category involves experimental factors with the emphasis here on flow rate fluctuations. In the case of the second category, control experiments have been performed by varying the manner in which reactant flow is regulated to the burner. To perform these experiments, active and passive diagnostic methods – high-speed image chemiluminescence and CARS (Coherent Anti-Stokes Raman Spectroscopy) have been employed respectively. In addition to testing the oscillatory behavior of conventional flames, special investigations into negative gravity flames form a part of the experimental campaign. These have been instrumental in providing a better sense of the manner in which the phenomenological hypothesis (buoyancy forces) proposed at the beginning of the investigation affects the premixed flame.

1.1. Report Outline

This thesis report has been organized in the following manner. Consisting of 8 chapters, the first chapter consists of the literature survey wherein the basis of the dual hypothesis is generated. Following this, the chapter discussing the research questions generated are then outlined. Next, prior to exploring the hypotheses proposed, the subsequent chapter focuses on the theoretical background necessary to comprehend the basis behind the concepts that will be expanded later. This includes fundamental terminologies of a premixed flame, controlling parameters and the mathematical model in which oscillations are considered. The next chapter on the diagnostic setup begins to delve into the instrumentation of the experiments that have been carried out during the data-gathering phase of the research. Once the experimental setup and theoretical background have been provided, chapter 5 is focused on the conditions under which the experiments have been carried out. Details such as the equivalence ratios, Reynolds number, and other critical parameters are provided at this stage. Following the post-processing of data gathered during the experimental phase, the next chapter (Chapter 6) involves an explanation of the results and observations made from the experimental campaign. Such results include the frequency analysis of the flame front oscillations, thermometry trends in accordance with the mathematical model etc. Following these results and discussions, the efforts performed towards mitigating the presence of these low frequency oscillations is elaborated within chapter 7. In closing the report, the final chapter (Chapter 8) provides the concluding arguments and a proposal for future recommendations that can be implemented to mitigate and explore additional causes of such low-frequency flame front oscillations.

2

Literature Review

The earliest report of low-frequency flame front oscillation comes from the work performed by Markstein [5] during an investigation of flame instability in laminar premixed flames. Research preceding this paper such as the works performed by Damkohler [6] and Shchelkin [7] had repeatedly concluded shear instabilities to be the reason. This conclusion was mainly due to the use of turbulent flame behavior as an analogy for laminar premixed flames. An example of one such work performed during this initial phase of investigations is the efforts by Damkohler [6] towards investigating laminar and turbulent premixed flames. This has been shown in figure 2.1 along with the respective burner diameter at which such results have been obtained. In the years that followed, experiments such as [8] performed at

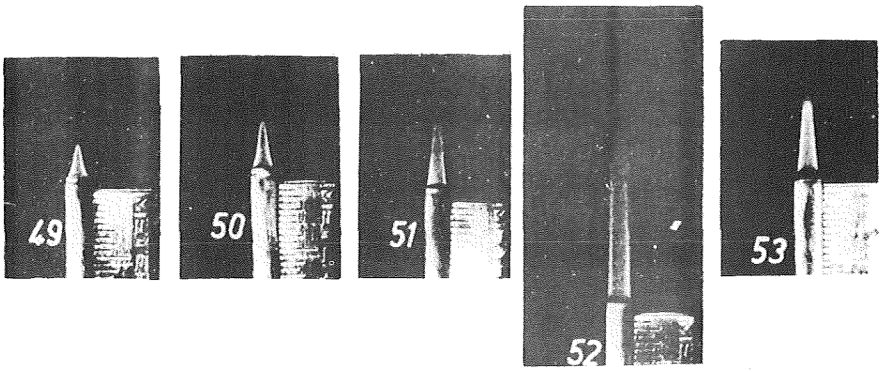

Figure 2.1: Propane-air premixed flame under a range of Reynolds numbers (laminar to turbulent conditions. Note that the numbers indicate the serial number of the particular flame experiment. These show variation in flame shape with changes to flow conditions under constant mixture ratios - [6]

low Re numbers with negligible turbulence have shown that such oscillatory behavior is still present. Following these contradictions, Markstein sets forth experiments to generate oscillations data. While the above-described research had detected flame instabilities, it is important to outline the reasons for addressing the issue. A contemporary paper on the effect of low-frequency oscillations is presented in the investigations by Crocco [9] focusing upon liquid propellant rocket motors. Attributing the cause to pressure variations within the combustion chamber, experiments were performed to control for propellant flow rate fluctuations and isolate a single cause. In addition to practical systems such as gas turbines and rocket engines, academic investigations of Putnam [10] and Nakanishi [11] into efficient combustion have also been affected by the presence of these instabilities.

Having established the problem under discussion, the reasons and solutions for these oscillations proposed until now can be explored. The experiments conducted by Kimura [12] are designed around the hypothesis that laminar jet-flow instability is the reason for flame-front oscillation. By measuring temperature and velocity fields in and around a laminar jet flame, perturbation data for these two metrics were analyzed. The researcher uses a form of PIV (Particle Image Velocimetry) to track velocity gradi-

ents around the flame front. Proceeding along a chronological order, the next hypothesis on a cause of oscillation is presented in [13]. Here, the phenomenon of 'pipe organ oscillation' is attributed as the general description of the process that is leading to Bunsen flame instability. While exclusively focusing on turbulent flames, when the frequency of thermal oscillations coincides with the natural frequencies of the burner tube, resonating tones are produced throughout the flame holder. Thus far, the two lines of reasoning proposed for flame instability fall into distinct categories. The explanation provided by [12] falls into causes based on experimental issues. On the other hand, the interpretation proposed by [13] refers to phenomenological reasons for flame-front oscillation.

Finally, the primary phenomenological hypothesis using buoyancy forces that was first proposed by Cheng and Bedat [14] is now outlined. In brief, the definition of buoyancy as employed here originates from the presence of density gradients surrounding the flame front as a result of the temperature difference between the ambient air and the flame. In the aforementioned investigation, Using a v-shaped flame for its one-dimensional nature, a combination of laser schlieren and PLIF (Planar Laser Induced Fluorescence) techniques were set up to probe spatial and temporal changes. Such an approach represents a workflow that is followed within the investigative effort of this thesis as well. To affect the buoyancy forces surrounding this flame front, Cheng [14] and colleagues have varied the Reynolds number (Re) and thus indirectly affecting the Richardson number (Ri). However, this examination of buoyancy was taken to its extreme with the design of an inverted burner. For the experimental hypothesis, the decision was made to study flow rate fluctuation as the primary cause. While the selection of buoyancy forces as a possible cause is supported by extensive literature, the investigation into flow rate variation as a contributor to low-scale frequency oscillations is more exploratory in nature.

Based on the considerations thus far, this thesis focuses upon buoyancy as a phenomenological reason and flow rate variations as an experimental reason. Having distilled the line of research into these two categories, contemporary works along these lines were required to understand the 'state of the art' in the respective fields. For example, one such report in the experimental category comes in the form of an investigation into reactant velocity changes affecting the stability of conical premixed flames [15]. Here, they replicate naturally occurring fluctuations in flow velocities by employing a sinusoidal frequency of fixed properties. Alternatively, a contemporary investigation into the phenomenological reason for buoyancy is the study by Krikunova [16] discussing flame-front oscillations in different flame shapes using high-speed chemiluminescence. It suggests that the dynamics along the flame front can be attributed to Kelvin-Helmholtz vortices in its immediate surroundings. These vortices are attributed (indirectly) to the presence of buoyancy forces. While not studying conical flames themselves, comparisons were made using m-shaped and v-shaped flames, as they are relatively easier to diagnose. This is because the one-dimensional nature of such flame structures ensures a lack of overlap between multiple layers of the flame. The reports made thus far deal with the chronology of observations made in the case of low-scale flame-front oscillatory behavior. However, the first indications of this phenomenon leading to this thesis topic come from the thermometry analysis performed by Castellanos et al [3]. By employing high-accuracy CARS spectroscopy across a partially premixed flame, low-frequency oscillations in the range of 10-13 Hz were captured. In the context of such thermometry work, the difficulty of probing regions within the flame-front reaction zone with high spatial resolutions is made difficult by such oscillatory behavior. As a result, contemporary reports to verify this behavior along with probable cause were sought. Investigations carried out by Barros [17] also showed frequencies of a similar range (9-10 Hz) but do not provide a core cause. It is under these circumstances that a more thorough search into the history of such oscillatory phenomena and the numerous reasons proposed for their presence was reviewed during the literature study phase of the thesis.

3

Research Questions

What factors are to be considered to stabilize low-frequency flame-front oscillations within Bunsen flames?

While such a question cannot be answered directly, certain sub-questions can be generated as stepping-stones. These are now listed in successively greater detail. Technically, it should be possible to answer the main research question upon providing an answer to these listed sub-questions.

1. Are the origins of these instabilities purely due to phenomenological reasons or due to experimental uncertainties?

2. Is it possible that these oscillations are produced due to a combined interaction of the former and latter?

3. If either of the above statements is true, are there experiments from previous literature that can be adapted to verify such a hypothesis?

4. Among physical phenomena, which ones are the most associated with flame front instability?

5. In the case of experimental reasons, what are the components of a diagnostic setup that are susceptible to such uncertainties?

6. What canonical flames are most suitable for testing such a prospective burner design? Are there experimental conditions that best depict possible reductions in flame-front oscillations?

Although the first half of these questions have been answered during the literature study phase, the resulting answers have generated the need for performing the experiments that are now outlined in further sections of the report.

4

Theory

Since the region of interest in this investigation is the behavior of the flame front, a clear definition of this part of the flame must be made. A simple way to do this is by observing the structure of a laminar premixed flame. Here, the structure refers to a cross-section of the flame in terms of the concentration of its components such as the fuel, oxidizer, and product gases. In addition to the reactants and products, the change in temperature at various regions in and around the flame is also shown alongside the variation in concentrations. The structure of a conical bunsen flame is now shown in figure 4.1.

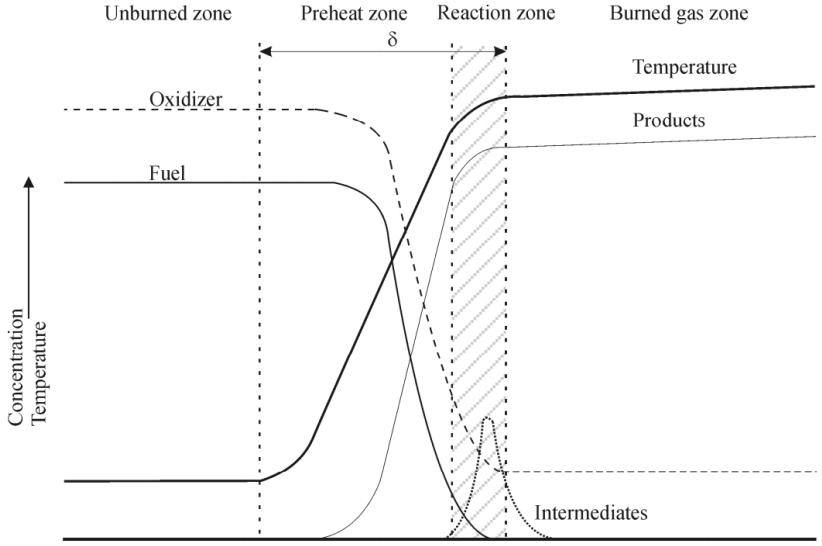

Figure 4.1: Structure of a laminar premixed flame [18]. The three zones of the flame - unburned reactants, reaction zone, and the burned gases are shown along with the reaction zone which is integral to chemiluminescence based diagnostics employed during this investigation

With this schematic in mind, we can now define a specific region that will be treated as the flame front for the rest of this investigation. Observing the change in temperature as we move from the ambient surroundings (extreme left) to the center of the flame (extreme right), a steep temperature gradient is visible. However, this temperature gradient is limited to two zones that are termed here as the preheat and reaction zones. Outside these regions, the temperature as well as the concentration gradients are negligible. If we observe the events within this region, a smaller transient event can be seen in the form of intermediates. The 'intermediates' here refer to the short-lived radicals that are continuously generated during the chemical reaction that is responsible for converting a fuel (methane) and oxidizer (air) into product gases. Among these intermediates, some notable ones are of interest to us in this investigation such as CH and C_2 radicals. It is in fact the presence of such radicals that is responsible for the

production of the luminous region that is clearly visible to the naked eye. By referring to the flame structure schematic once again, it is clear that the intermediates fall exclusively within the reaction zone of the flame. Unlike the unburned zone or the burned gas zone, this luminous part of the flame lends itself to visual analysis. It is based on this idea that the selection of high-speed image chemiluminescence was made as the primary diagnostic tool. A more in-depth explanation of the connection between the diagnostic technique and the presence of these radicals is explored within the chapter discussing the diagnostic tools used in this investigation. Now that the region under investigation has been clearly defined, the chemical process and parameters responsible for the flame can be described.

4.1. Flame fundamentals

Let us begin by considering the chemical reaction responsible for producing combustion. Since the flame employed here is a methane-air premixed flame, the equation below describes the reactants, products, and energy released during the process.

$$CH_4 + 2(O2 + 3.76N2) \rightarrow CO2 + 2H2O + 7.52N2 \Delta H = -810 kJ/mol \tag{4.1}$$

For every mole of methane, two moles of diatomic oxygen and 7.52 moles of diatomic nitrogen are required to complete the combustion process. At the end of the equation, the value of 810 kJ/mol refers to the amount of heat energy that is released for every mole of methane being consumed within the reaction. However, the disclaimer to be made at this stage is the theoretical nature of this equation. This means that the ratio of the number of moles between a fuel (CH_4) and oxidizer ($O_2 + 3.76N_2$) is set at the ideal value to allow a stochiometric reaction to occur. We can quantify this special ratio in the following manner:

$$Stoch_{ratio} = \frac{Fuel_{moles}}{Oxid_{moles}} \tag{4.2}$$

While the number of moles may be useful when discussing reaction equations, a more practical metric of the amount of fuel and oxidizer is the molar fraction. It is defined as the ratio of the number of moles of a specific species to the total number of moles for the reactants. The mathematical definition is as follows:

$$M.F_{fuel} = \frac{n_{CH_4}}{n_{total}} \tag{4.3}$$

$$M.F_{oxid} = \frac{n_{N_2} + n_{O_2}}{n_{total}} \tag{4.4}$$

Next, the mass fractions of the fuel and oxidizer now allow for variations in the mixture ratio to be quantified. A single term to enclose both of these fractions referred to as the equivalence ratio can now be put forth. Denoted conventionally by the symbol φ, it is defined as the ratio of the molar fractions of the fuel to that of the oxidizer. To make this term more accessible, the following derivation can be performed.

$$F.A_{ratio} = \frac{M.F_{fuel}}{M.F_{air}} \tag{4.5}$$

$$F.A_{ratio} = \frac{fracn_{CH_4} n_{total}}{\frac{n_{N_2}+n_{O_2}}{n_{total}}} \tag{4.6}$$

$$F.A_{ratio} = \frac{n_{CH_4}}{n_{N_2} + n_{O_2}} \tag{4.7}$$

$$\phi = \frac{F.A}{F.A_{stoch}} \tag{4.8}$$

Using the expression developed in equation (4.7), the expression of equivalence ratio as shown in (4.8) can be expanded as follows:

$$\phi = \frac{\frac{n_{CH_4}}{n_{N_2}+n_{O_2}}}{\frac{n_{CH_4}}{n_{N_2}+n_{O_2}\ stoch}} \tag{4.9}$$

The above expression defines the equivalence ratio in terms of the number of moles of fuel and oxidizer comparing a specific condition to the stochiometric conditions. Alternatively, this term can also be

written in terms of the actual mass of fuel and oxidizer. In doing so, the equivalence ratio in terms of the mass of fuel (CH_4) and oxidizer (O_2, N_2) can be written as follows:

$$\phi = \frac{[\frac{m_{CH_4}}{m_{N_2}+m_{O_2}}]_{expr}}{[\frac{m_{CH_4}}{m_{N_2}+m_{O_2}}]_{stoch}} \tag{4.10}$$

In this equation above, the numerator term is sub-scripted as 'expr' to denote the experimental fuel-air mixture in contrast with the stochiometric mixture ratio that is theoretically known. Now that the controlling parameter has been explained, the subsequent sections within this theoretical explanation will discuss the predicted effects that take place upon changing the equivalence ratio as well as the flow conditions of the reactant mixture. With this, the requirements for combustion in general as well as the parameters by which it is controlled have been explained. Now, the specific case of the laminar premixed flame can be described along with the dynamics involved in sustaining such a flame. The laminar premixed flame is one among two types of flames that can be generated based on the manner in which the fuel and oxidizer are allowed to interact with each other. Premixed combustion involves the mixing of fuel and oxidizer prior to ignition while non-premixed combustion undergoes a diffusion process wherein the fuel and oxidizer interact with each other post-ignition. This creates visually distinct features that differentiate these flames as shown in figure 4.2

Figure 4.2: Visual differences between a premixed shown on the right and an example of a diffusion flame shown on the left. Note the characteristic difference in the color of the flame which is a direct result of the manner in which the reactants interact with one another during combustion

In addition to a flame being classified based on the manner of reactant interaction, the flow conditions of the reactant mixture are also used in conjunction to classify a flame as either a laminar or turbulent flame [19]. In this research thesis, the oscillations studied pertain only to laminar premixed flames. Conventionally, this type of flame is generated using a Bunsen-type conical flame [19]. At this juncture, it is vital to note that a laminar premixed flame is not limited to a specific shape. The configuration of the burner employed as well as the stabilization mechanisms used contribute to the shape of the flame front. Canonical burner designs that are substantially more sophisticated include McKenna burners [20], annular co-flow burners [21] etc. Focusing upon the conical bunsen flame, the following diagram in figure 4.3 depicts the shape of such a flame with an inset vector representation showing the forces at play around the flame-front boundary itself. As indicated, the reactants (methane and air) are piped into the burner via separate entry points before being mixed prior to ignition. The arrows labeled Vu within the inset diagram represent the flow velocity of the now premixed mixture of

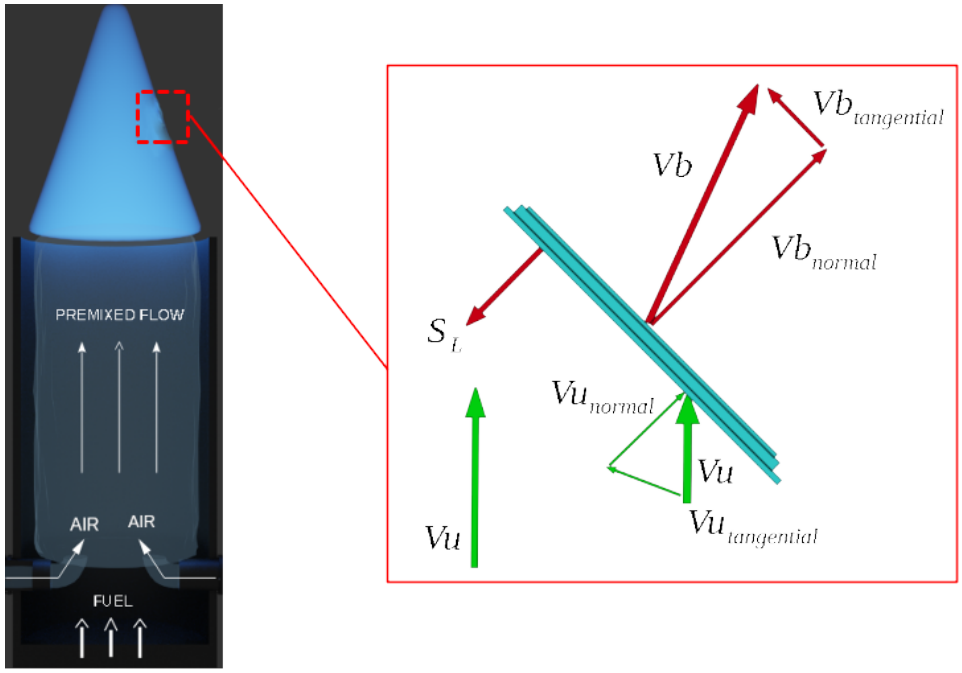

Figure 4.3: Representation of a conical premixed flame with a depiction of interacting forces at the flame-front boundary. The inset diagram on the right shows the balancing effect created by the tangential component of the reactant flow velocity $V_{utangential}$ and the normal component of the laminar burner velocity $V_{bnormal}$

reactants. Since the phenomenon of combustion involves fluid dynamics concluding with a chemical reaction, the conservation laws such as mass conservation and momentum conservation have to be obeyed. This is represented by the balanced vectors S_L and Vu_{normal}. Here, the term S_L refers to the laminar burning velocity, and Vu_{normal} refers to the normal component of the reactant flow velocity. Thus, the conical shape of the flame front is a result of the balance between the forces associated with Vu_{normal} and S_L. The simplest method to generate such a flame as described above is the use of a Bunsen burner. This is a common approach to generate premixed, as well as diffusion flames without the requirement for complex burner designs [22]. In comparison to burner configurations mentioned earlier, the design shown in figure 4.3 is the most simple to construct. A primary characteristic of this flame is its conical inner zone. The shape can be explained as a result of the imbalance between the resultant flow velocity Vu and the laminar burner velocity S_L. As a result of this imbalance, such premixed flames prefer to maintain their shape independent of the orientation of gravitational forces. This becomes especially relevant when experiments involving flame inversion are performed.

4.2. Interaction between flame and ambient surroundings

With an understanding of the origins of a conical premixed flame, its interaction with the ambient surroundings can now be explored. Ideally, the dynamic forces within the flame along with the ever-present forces of gravity and atmospheric pressure is an important factor to consider [23]. In reality, the interactions between the flame front and the ambient environment require a deeper exploration of these above-mentioned factors. Unlike a theoretical flame, a practical premixed flame is prone to fluctuations as a result of experimental errors or naturally occurring phenomena. Consequently, the factors associated with such disturbances are classified in the same manner [24].

Let us begin by describing the experimental interaction between flow rate fluctuation and flame front oscillation in qualitative terms. While premixed flames may have a unified flow rate for the reactants prior to ignition, this quantity is directly affected by the independent flow conditions of the fuel (CH_4) and oxidizer (Air). While flow velocities of the individual reactants may be a better term to use, the all-encompassing idea of flow conditions implies that the effects of flow rate variations due to leakages and constraints within the piping system are not neglected. At first, these nuances of definition appear to be trivial. However, by considering the flow rate as a whole, one can avoid the complications of

accounting for changes in the area of cross-section or flow velocities within the control system. In addition to actual variations in flow rates, perceived changes to flow rates must be considered as well. This may occur due to built-in uncertainties within the individual flow control apparatus assuming that the range and sensitivity of the devices employed are appropriately selected. During some preliminary tests to show the presence of such low-frequency instabilities, analog flow controllers were employed to regulate the fuel and oxidizer. It is within these analog flow regulation systems that the presence of flow rate fluctuation can be found.

4.3. Working principle of the flow control system

4.3.1. Analog rotameter

To understand its origins, the working principle of an analog controller is required to be understood. The following diagram in figure 4.4 represents the cross-section cutaway of a float-based variable area glass rotameter. The regulation of the fluid is achieved by the dynamic between the drag force of the

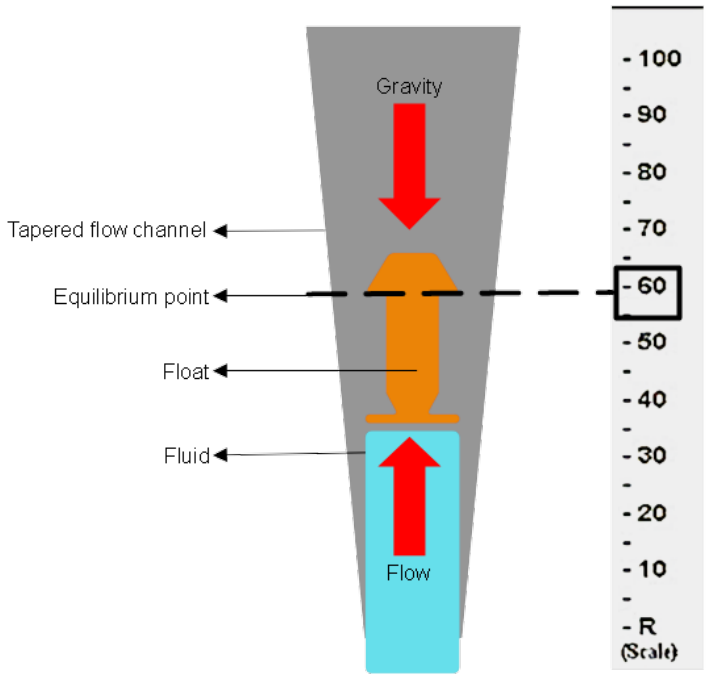

Figure 4.4: Cut-away diagram of a float-based analog rotameter with the dynamic equilibrium of gravity and fluid flow depicted. By calibrating the position of the float for a given flow rate, a scale of measurements can be made for a given fluid

fluid experienced by the float against the gravitational force acting on the float in the opposite direction. The tapering of the flow channel creates a variable area for the fluid to flow through. The position of the float within the tapered tube is directly proportional to the flow rate of the fluid. The taper of the tube allows for a larger area for the fluid to flow through at higher flow rates and a smaller area for the fluid to flow through at lower flow rates, creating a linear relationship between flow rate and float position. As is evident from this explanation, the process of flow regulation here is entirely mechanical in nature. Furthermore, there is no way to make minor adjustments once a particular flow rate is selected by means of a simple valve. It is within the operation of these components that the problem of uncertainties in the flow rate originates.

4.3.2. Digital mass flow controller

With this understanding of the inner working of the flow regulation setup used thus far, the decision to employ and assess the use of a higher-accuracy control system with a feedback loop was made. To do so, a thermal mass flow control system using a bypass valve design was employed. A thermal mass

flow controller with a bypass design uses a thermal sensor to measure and control the flow rate of a gas. By placing a heating element between two thermocouples, the change in temperature of the fluid as it passes through the bypass line is used to compute the rate of mass flow through the controller. Using this information, the software onboard the controller alters a solenoid valve to make corrections as needed once a flow rate value has been set by the user.

Now, we can move on to a description of the phenomenon based source of flame front fluctuation in the form of buoyancy forces. Please note that these explanations are only qualitative in nature and will be followed by a mathematical description of the events. As proposed by Cheng and Bedat [14] is the effect of buoyancy forces as a result of the subtle density variations occurring in the immediate vicinity of the flame-air interaction zone. Changes in the density of the flame products as a result of a continuous chemical reaction within as opposed to the static conditions found in the surrounding atmosphere result in a density gradient field in all directions around the conical flame. As a result of any one or combination of the aforementioned effects, the flame front begins to oscillate. Upon observing this phenomenon for the first time, a low-fidelity image-based analysis of the flame was performed. The procedure by which the frequencies of the oscillations were extracted is detailed within the section on the primary experimental setup of the project. The exact steps connecting the origin to the low-frequency oscillations are dependent on the final cause that is concluded within the report. With these simple descriptions in mind, the quantification of these two hypotheses can now begin.

4.4. Quantifying instability in flames

In order to predict the frequency of the oscillations that can occur under a specific condition (equivalence ratio Reynolds number), the two primary approaches – experimental and phenomenological will require separate methods of quantifying according to their individual characteristics.

4.4.1. Oscillation as a function of buoyancy

We first begin with a method to model the effects of buoyancy forces as they show up within laminar premixed flames. To begin quantifying oscillatory instabilities, the metrics involved with the reactants prior to and post-combustion is provided below. In addition to the metric, the justification for their use in these mathematical explanations is also sought by way of these definitions.

- **Reactant flow rate:** Describes the mass flow rate of the reactant mixture as it passes through the burner outlet towards ignition. It is denoted here by Q_r.
- **Reactant velocity:** As per the laws of mass conservation, the velocity associated with reactant flow is an independent metric when discussing non-dimensional flow variables such as the Reynolds number or the Richardson number. Here, it is denoted by u_r.
- **Reactant density:** This quantity is an average non-weighted value between the density of the fuel in use (CH_4) and that of the oxidizer (Air) [14]. In conjunction with the density of the ambient air that surrounds the flame, it will play an important role in deciding the degree to which density gradient across the flame front may cause instabilities [16]. It is represented using ρ_r.
- **Burner diameter:** The diameter of the burner is integral in deciding the Reynolds number of the reactant flow. During the course of the experiments, a change in burner diameter was necessitated in order to reduce reactant flow velocities while maintaining a specific Reynolds number. The diameter is represented using D.
- **Oxidizer viscosity:** On the basis of certain mathematical models demonstrated in the next section, the use of the dynamic variant of the viscosity of the oxidizer (air) is integral to the equations involved [14]. This is represented using μ.
- **Heat release ratio:** In relation to the discussion on density gradients, this expression is integral in connecting thermal and fluid flow quantities. It is represented within this report using τ and is computed as shown below.

$$\tau = [\frac{T_p}{T_r}] - 1 = [\frac{\rho_p}{\rho_r}] - 1 \tag{4.11}$$

  Here, the terms T_p and T_r refer to the temperature of the product gases and unburnt reactants respectively.
- **Product Density:** In addition to the previously mentioned ρ_r, the product density ρ_p refers to an average value composed of combustion products resulting from the Bunsen flame.

- **Adiabatic flame temperature:** This quantity is defined as the temperature that would be measured within the flame-front under the ideal conditions of zero heat losses with respect to its surroundings.
- **Ambient Temperature:** This is defined as the temperature of the environment in which the flame is sustained. With the exception of inverted conical flames, the temperature of the reactants prior to combustion will match the ambient temperature of the surroundings. The disagreement between reactant and ambient temperature occurs for inverted flames due to the preheating of the fuel-air mixture that occurs as a result of the natural inclination of the flame plume to burn in the upright orientation. Thus, apart from this exception, the former generalization is still valid for conical flames.

The literature study performed in the previous section is forms the first step in forming a basis for connecting the unsteady spatial motion of the flame-front with the forces related to buoyancy. We begin with the formation of non-dimensional numbers, specifically the Reynolds number and the Richardson number. While the Reynolds number is a widely used variable when studying fluid flow, the definition used in this context is derived as follows.

$$Re = \frac{\rho_o \cdot d \cdot u_r}{\mu_o} \tag{4.12}$$

Here, the ρ_o and μ_o represent the density and dynamic viscosity of the oxidizer. Having setup one end of the model, the Richardson number is defined below in compliment to the Reynolds number.

$$Ri = \frac{\rho_o \cdot g \cdot d^2 \cdot \tau}{\mu_o \cdot u_r \cdot (\tau + 1)} \tag{4.13}$$

Before proceeding to bridge these terms, let us define each of the non-dimensional number in a qualitative manner. The Richardson number can be interpreted as the ratio between the buoyancy term and the flow shearing term. The buoyancy term is calculated as the multiple of the density gradient with respect to position and the gravitational acceleration experienced at the given position. Mathematically, it is defined as follows:

$$B = g \cdot \frac{\delta \rho}{\delta z} \tag{4.14}$$

The shearing term on the other hand is defined as the multiple of the velocity gradient with respect to position and the density of the flow at that given position. Mathematical equation is as follows:

$$S = \rho \cdot \frac{\delta u_r}{\delta z} \tag{4.15}$$

Thus, the idea of density gradients with respect to the position of the flame-front affecting the stability of the conical flame is now made more concrete in the form of this non-dimensional quantity (Richardson number). To tie these two quantities together, a third and final non-dimensional quantity is still required. This term is the Strouhal number. In the context of flame front oscillation, [14] defines the Strouhal number in the following manner:

$$St = \frac{\nu^2 \cdot d^2}{u_r^2 \cdot (\tau + 1)} \tag{4.16}$$

Qualitatively, this non-dimensional quantity is stated as the ratio that correlates flow rates with the frequency of oscillating mechanisms. Thus, having setup all three of the primary variables, the model to bridge these terms are now presented below.

$$\frac{St^2}{Ri} = (0.0018)(Re)^{2/3} \tag{4.17}$$

Reducing the abstraction of the equation above, we can re-write it such that the frequency of oscillation can be extracted as a numeric value. This derivation is now down below:

$$\frac{[\frac{\nu^2 \cdot d^2}{u_r^2 \cdot (\tau+1)}]^2}{\frac{\rho_o \cdot g \cdot d^2 \cdot \tau}{\mu_o \cdot u_r \cdot (\tau+1)}} = 0.0018 \cdot [\frac{\rho_o \cdot d \cdot u_r}{\mu_o}]^{2/3} \tag{4.18}$$

Having replaced all of the non-dimensional terms with their full-length representation, let us begin to isolate the frequency term v from the other physical variables.

$$[\frac{\nu^2 \cdot d^2}{u_r^2 \cdot (\tau+1)}]^2 = (0.0018) \cdot [\frac{\rho_o \cdot d \cdot u_r}{\mu_o}]^{2/3} \cdot [\frac{\rho_o \cdot g \cdot d^2 \cdot \tau}{\mu_o \cdot u_r \cdot (\tau+1)}] \tag{4.19}$$

$$\nu = [\frac{0.0018 \cdot u_r^3 \cdot \rho_o \cdot g(\tau^2+\tau)}{d^2 \mu_o} Re^{2/3}]^{1/4} \tag{4.20}$$

Equation (4.20) now represents the distilled version of the aforementioned model in terms of oscillation frequency. Although the Reynolds number was previously deconstructed for the purposes of derivation, it is still a quantity that is set during the experimental process. This implies that the Re value is more useful as a direct quantity instead of breaking it down to its constituent components. Having defined a model in terms of oscillation frequency, we are now ready to make use of this equation when the two dominating factors – fuel-air ratio and Reynolds are controlled separately in the experiments described in subsequent sections. Having outlined a model to describe buoyancy-based oscillations, we can switch toward the flow rate fluctuation hypothesis.

4.4.2. Oscillation as a function of flow rate fluctuations

This approach requires an empirical correlation between the fluctuations observed within the mass flow controllers (changes to the flow rate with time) and the frequency at which the flame front itself oscillates. Since this hypothesis has to be tested for the first time, the correlation is defined as follows.

$$\nu_f = F_{co} \times \nu_c \tag{4.21}$$

Here, the terms ν_f and ν_c refer to frequency peaks obtained from the spectra of the temporal oscillations within the flame and controller respectively. To allow for a proportional variation between the two quantities, a correction factor F_{co} is inserted as well. To extract data from the flow controllers, the response time and data points at specific intervals are retrieved using the inbuilt event log system for both controllers (fuel and oxidizer). While it is possible that any influence due to buoyancy may affect the results obtained in this approach, control experiments were also performed using a self-designed inverted Bunsen burner. The implementation of such a control experiment is based upon the work performed by Cheng [14] wherein a custom-designed premixed flow burner was employed. A description of the design employed in the reference along with the differences in the design adopted in this research project is outlined within the section on the experimental setup.

5

Diagnostic Setup

5.1. Selecting a diagnostic technique

With the goal of measuring the frequency of oscillations within the flame front, it follows that any diagnostic technique chosen must involve the detection of the spatial position of the flame front over a given time period. To this end, a survey of techniques employed within the previously studied literature was inspected as a starting point. A common trend observed among contemporary as well as early reports of oscillatory instabilities is the use of image-based analysis. These reports range from Damkohler [6] employing analysis of physical photo positives recorded over a period of time to the more recent works using digital image processing [16]. Owing to the low-frequency nature of the phenomenon involved, it is clear that the use of flame imagery as a source of spatial position data for the flame front is sufficient to extract frequency data. However, it must also be noted at this stage that a secondary diagnostic tool in the form of CARS spectroscopy has also been utilized as a part of the experimental campaign. This has been done with the aim of extracting thermometry data for some of the flame configurations outlined during the experimental campaign. While the use of photographic imaging has been chosen based on earlier research, the employment of CARS spectroscopy has been left to be explained in later chapters. The subsequent sections of this chapter will now describe the manner in which the two diagnostic techniques – image processing and CARS spectroscopy were implemented during the analysis. It will also include the various challenges and shortcomings faced during their utilization.

5.2. Image chemiluminescence – Primary diagnostic technique

5.2.1. Working principle

Prior to describing the implementation, the fundamental principles behind this technique have to be explained first. The use of photographic sequences to determine the spatial position of the flame front is a non-intrusive line-of-sight procedure. The technique is cost-effective in terms of instrumentation in relative terms. Additionally, the simplicity of the setup and lack of calibration procedures also give this approach a decisive advantage over other techniques in terms of acquisition time. The following diagram in figure 5.1 represents the most basic components necessary to perform image processing of a flame.

While the actual setup involves a more detailed placement of these components, the exact setup used within the experiment will be depicted later. Finally, the quality of data generated from this method can be improved in situ by the use of additional optical elements. However, care must be taken in employing them as they can have detrimental effects on other qualities of the image begin acquired. While the fundamental components can be simplified to the flame, imaging system, and focusing optics, there are some challenges that have to be overcome in order to make practical use of the acquired images. Conventionally, the use of CCD (Charge-coupled device) has been the primary way of acquiring images as a result of their high sensitivity. While the earliest digital imaging approaches have favored the use of CCD sensors, even contemporary works such as the investigation into combustion chemiluminescence by Trindade et al [25] have still favored the use of CCD due to their previously

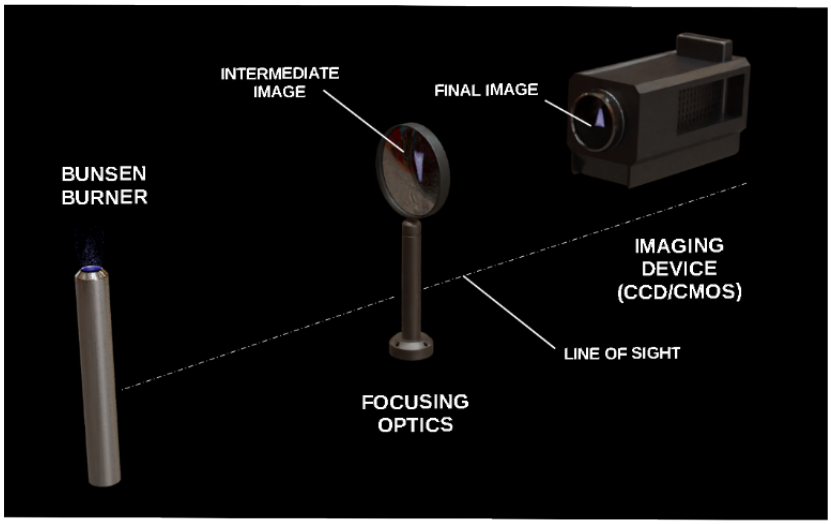

Figure 5.1: Fundamental components for image chemiluminescence. While components such as the focusing optics may vary based on the requirement of the experiment, the concept of image chemiluminescence in its raw form can be performed without the use of such optical systems apart from an imaging device

mentioned advantages. However, the inherent problems with this technology such as lower refresh rate and presence of artifacts have to be considered [26]. Alternatively, the advent of CMOS sensors within the field of imaging has also been explored. With the capability to achieve higher temporal resolutions and the ability to address individual pixels within the image frame, it initially appears to have solved the problems posed by the use of CCD sensors. On the other hand, the reduced sensitivity to light and the lack of dynamic range leading to the presence of noise and over-saturation is a problem that has to be addressed before performing any form of further analysis. In the case of this investigation, a compromise between these two systems in the form of an sCMOS (scientific CMOS) sensor has been chosen [27]. As is evident from the discussion above, both CCD and CMOS systems have favorable properties while their respective disadvantages can be countered by choosing this middle option. A scientific CMOS sensor-based camera allows for achieving a high temporal resolution while maintaining sufficient spatial resolution, low noise, and a sufficiently wide dynamic range. This has been achieved by employing dual amplifiers to reduce the noise of the output images. Additionally, a dual analog-to-digital converter setup allows for refresh rates that are comparable to the performance of CCD sensors [27]. For the image chemiluminescence experiments in this thesis, the Andor Zyla 5.5 sCMOS camera exhibits these advantages against a CCD equivalent in the following comparative image of a standard 1951 USAF resolution chart as shown in figure 5.2. This is where the need for processing algorithms to compensate for the insufficient dynamic range as well as the presence of noise within the image was found to be necessary [28]. By a process of trial and error, an algorithm that is best fitting for the investigation at hand was formulated. After applying the processing algorithm, the actual computation of frequency data for specific flame conditions has been performed. The subsequent chapter on the methodology by which these diagnostic tools are employed can be referred to visualize the steps taken towards processing and the type of outputs that are produced by high-speed image chemiluminescence. With this overview of the primary diagnostic technique, we are now ready to describe the fundamentals of image chemiluminescence as a diagnostic tool.

Consider the following image of a conical Bunsen flame captured at close range as shown in figure 5.3. By manipulating the flow rate of the fuel (CH_4) and oxidizer (Air), a stochiometric mixture has been established for this particular case. Visual inspection of the flame reveals two distinct regions – an inner cone and an outer flame. The region of interest for image processing lies at the interface formed by the inner cone and the outer flame. To better understand the connection between this luminous

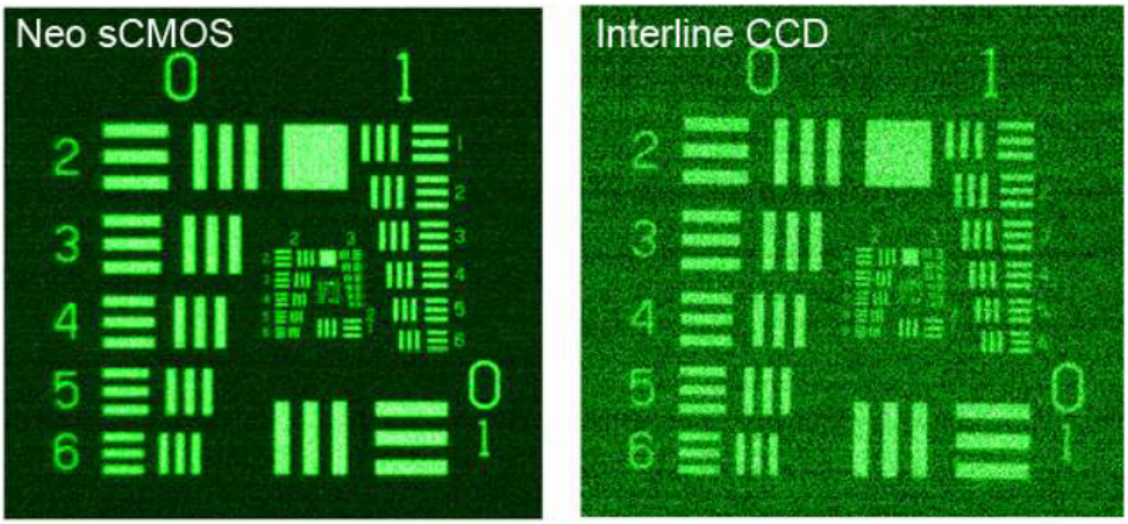

Figure 5.2: Comparing a Zyla Neo sCMOS sensor output (left) with an interline CCD sensor (right) [27]. In this comparison, the standard USAF 1951 resolution test chart has been used as a benchmark for reference.

region and the resulting frequency spectra, the flame structure during combustion must be examined. Taking a one-dimensional slice (as shown in dotted lines in figure 5.3) along this interface extending

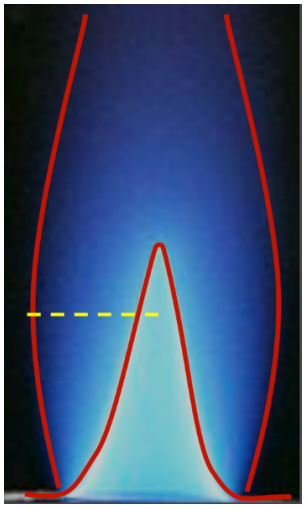

Figure 5.3: Stochiometric conical flame with marked regions and diagnostic slice. The interface between the non-luminous outer region and the luminescent core of the flame is the region where the diagnostic slice is placed during the analysis.

from the outer region to the center of the inner cone, the concentration and temperature data for the reactants and products at various points along this diagnostic line reveals the sub-steps taking place during the combustion process. A conventional way to depict this is now shown in the plot of a premixed methane-air flame structure as shown in figure 5.4. The diagram above depicts the changes in concentration and temperature of the flame as we pass through the various regions along the diagnostic slice marked in figure 5.3. These changes follow the numerous chemical reactions (including intermediate reactions) occurring within the respective regions to finally generate the combustion products at the end of the process. Focusing on the area between the unburned zone and the burned gas zone, one can find the region referred to as the reaction zone. This region (marked in figure 5.4) is the same as the luminous zone previously observed at the interface between the inner cone and the outer region of the flame. While the temperature is seen to progressively increase from left to right, the concentration of the fuel, oxidizer, and products change in accordance with the rules of combustion. Essentially, the concentration of fuel and oxidizer reduces as the temperature and concentration of products increase. In addition to these changes, a new quantity in the form of ‘intermediate’ substances is also generated

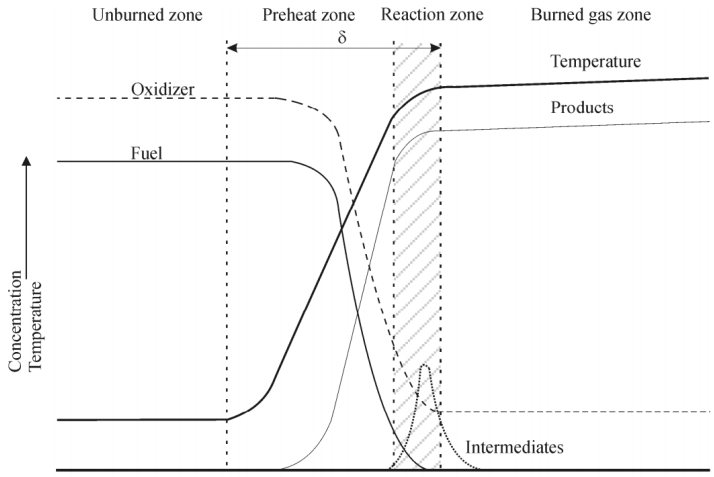

Figure 5.4: Flame structure schematic for a premixed laminar flame [18]. The short-lived radicals that are responsible for luminosity at the reaction zone are present within the region referred to as the intermediate zone in the diagram.

at the reaction zone. These intermediates are radical species generated by chemical reactions that form the sub-steps involved in converting reactants to products. The lifetime of these unstable species is very short relative to the final combustion products and acts as the basis for the mechanisms by which the chemical reaction is performed. Among the multitudes of species generated, some of the notable ones are OH, CH, C_2, and CN radicals.

The luminosity previously mentioned at the interface can be attributed to these intermediates generated over an extremely short time span. This is proven by the observation of spectral emissions within the reaction zone as depicted in figure 5.5. These emissions also referred to as Swan bands are the

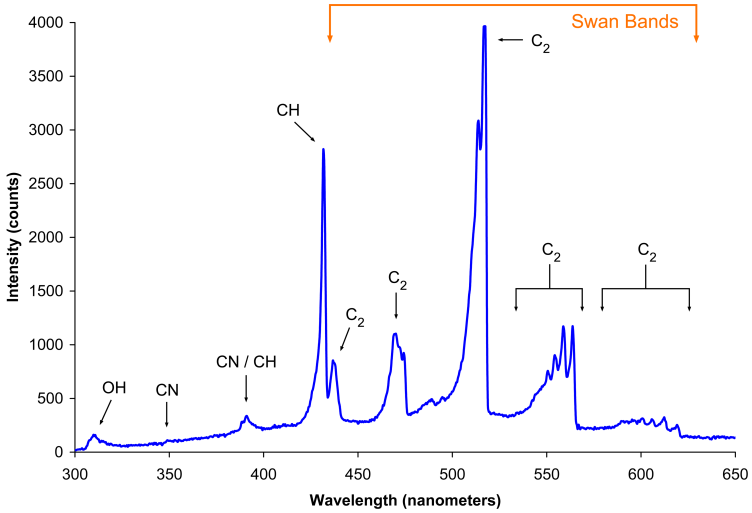

Figure 5.5: Radical emission spectra for a propane-air premixed flame (with Swan bands marked within the spectrum) - Please note that this is shown to depict the presence of intermediate radicals exclusive to hydrocarbon flames and does not include flames wherein hydrogen is used as a reactant

result of radical emissions generated during the excitation of hydrocarbon compounds [29]. In the case of this thesis, the source of excitation is the combustion reaction occurring within the reaction zone itself. Upon observing the wavelengths in which these excitations are present, it is clear that they are within the visible range of the electromagnetic spectrum. While there are other parts of the spectrum in addition to the Swan bands themselves, the in-situ additions to the basic instrumentation such as the

band-pass filter become very useful to isolate this spectral region of interest. Visually, such isolation will correspond to eliminating the outer region of the flame. Thus, a direct relationship can be traced between the presence of the radical species and the luminosity generated at the reaction zone. This implies that the visual tracking of the luminous zone can be used to record the spatial position of the flame front itself. This approach forms the basis of chemiluminescence-based image processing. Following the acquisition of flame-front images in this manner, the frequency data for each flame configuration is extracted using a post-processing algorithm that will be described in the subsequent section along with the instrument layouts attempted to achieve it.

5.2.2. Advantages and disadvantages

The advantage of combining chemiluminescence [30] with high-speed imaging can be summarized by the following points:

- Non-intrusive analysis of flame front (no physical probes used)
- Intermediates such as transient radicals are detectable via the luminous region
- Extremely simplified setup - Imaging systems can be replaced by human observers (if needed)
- Isolation of sensing optics from the flame burner is possible using fiber optics to avoid disturbances of the ambient surroundings due to the presence of human observers.

The disadvantages of using the above-mentioned diagnostic setup can be outlined as follows:

- Interference from luminescence data of outer cone regions of the flame (burned gas zones) especially in the case of axisymmetrical flames (conical flames)
- Requirement of processing algorithms to eliminate background information which in the case of flame analysis refers to the ambient surroundings.

5.3. CARS thermometry – Secondary diagnostic technique

Now that the fundamentals behind image chemiluminescence have been fully elaborated, the diagnostic approach used for the thermometry analysis within the experimental campaign can now be explained. Coherent Anti-Stokes Raman Spectroscopy is an in-situ non-intrusive laser-based diagnostic method that has found use in the field of combustion research [31]. However, it must be noted that the basic idea behind CARS has been in use following the advent of laser technology in determining quantitative scalar information such as temperature and concentration of gas-phase species [32]. The possibility of the involvement of temperature in linking buoyancy to low-frequency oscillation as explained in section 4.4 was of sufficient interest to invest efforts towards this analysis approach. Before the implementation of CARS can be described, the underlying principles involved will now be briefly mentioned.

Coherent Anti-Stokes Raman Spectroscopy (CARS) is a collection of techniques, each optimized for specific applications. This particular project uses a pure rotational hybrid femtosecond/picosecond (fs/ps) two-beam CARS setup to study chemically reacting gas-phase flows. The method preserves the benefits of time-resolved CARS by utilizing a narrow-band picosecond probe pulse that is preceded by a femtosecond broadband pump and Stokes pulse combination [3]. This approach circumvents the influences of non-resonant signals by providing sufficient temporal resolution while maintaining enough spectral resolution to detect the frequency domain. The high peak powers of these pulses, resulting from their brief duration, enable impulsive CARS signal generation, leading to more efficient excitation of the coherence in comparison to nanosecond CARS applications, resulting in higher signal levels [33]. This facilitates the study of matter under extreme conditions. In this investigation, the extreme condition of importance is the premixed flame undergoing low-frequency flame front oscillation. The decay of molecular coherence is a non-issue for this type of CARS diagnostics but it is mainly caused by collisions between molecules, leading to energy exchange. This phenomenon is also referred to as ‘collisional decay’ [34]. From a user standpoint, it is sufficient to understand that this process of decay has a detrimental effect on the resonant signal over time. This decay occurs on a time scale of a few hundred picoseconds. Thus, with a probe duration in the order of 4 to 5 picoseconds i.e more than an

order of magnitude reduction, the CARS signal generation happens on such a short time scale that the effect of the decay becomes a non-issue during combustion diagnostics.

The conventional approach of Coherent Anti-Stokes Raman Spectroscopy (CARS) involves the use of three incoming lasers to generate the output CARS signal. However, in this investigation, a modified technique referred to as the two-beam hybrid femtosecond pure rotational CARS was employed that utilizes only two beams. The following diagram in figure 5.6 shows the effect that these input and output beams have on the energy levels within the probe volume. This is possible as the pump and Stokes beams are temporally degenerate. This means that the pump and Stokes photons of different frequencies arrive simultaneously in time for the entire duration of the pump/Stokes pulse as a result of employing broadband laser beams in the process. This modification allows for some very significant simplification to be performed, one of which is that the pump and Stokes photons are spatially overlapped and automatically synchronized at the measurement location. The shorter the duration of the pump and Stokes pulses, the more difficult it becomes to synchronize these pulses in the time domain, making this technique substantially more advantageous when employing ultra-short laser pulses in the order of femtoseconds. Additionally, this spatial and temporal overlap of the pump and Stokes pulses makes the two-beam CARS method less susceptible to signal loss due to beam-steering compared to its three-beam counterpart. Another advantage is that the resulting CARS signal propagates alongside the probe pulse, making it easier to align the output detector. Thus, by crossing the two laser beams within the probe volume, a third beam (CARS signal) is generated as the output. This signal is then acquired by the detector placed at the appropriate location. The strength of such an output signal can be described using the following expression [35]:

$$I_{CARS} \sim \omega_{CARS}^2 \cdot I_{Pump} \cdot I_{Stokes} \cdot I_{Probe} \cdot |X_{CARS}|^2 \cdot z^2 \cdot (\frac{sin(\Delta kz/2)^2}{\Delta kz/2}) \tag{5.1}$$

Here, the ω_{CARS} represents the angular frequency and is conventionally referred to as the carrier frequency. The 'I' in expression 5.1 refers to the intensities of the input and output beams. Finally, the X_{CARS} refers to the third order susceptibility [36] of the CARS signal, the term 'z' refers to the probe volume length and the expression Δk refers to the phase mismatch. This mismatch is addressed by a phase matching scheme as it is important to determine the direction in which the CARS signal is output from the probe volume. In the case of a two-beam implementation of CARS, it is important to understand that the direction of the output CARS beam is dependent primarily on the crossing angle between the pump/Stokes and probe beam. However as mentioned earlier, the advantage of the CARS implementation here leads to the probe beam being in close alignment with the CARS beam for most crossing angles [35].

5.3.1. Connecting CARS spectra to temperature

Now that the way in which a CARS signal is produced has been explained, the theoretical basis to link the spectra that are obtained to the temperature of a target species can be elaborated. As described in chapter 4, any hydrocarbon flame involves the continuous presence of nitrogen molecules throughout the combustion process. Naturally, this makes it ideal as a species that can be used to track the change in parameters occurring during the process [37]. In the case of this investigation, the parameter of interest would be the temperature of a select region within the flame. This link between temperature and the N_2 molecules can be clearly seen in the following figure (figure 5.7) showing the rotational spectra of N_2 for different temperature cases. Clearly, the population distribution for various rotational energy states appears to be temperature sensitive. Mathematically, this spread of excited rotational energy states resembles a typical Boltzmann distribution [38]. Armed with this knowledge, it is now possible to generate a theoretical population distribution for various temperature cases for a specific species (in this case N_2). By comparing the actual spectra obtained by the rotational CARS setup, a comparative analysis can then be made to extract the exact temperature at which the experimental and synthetic distribution shows the closest match. The implementation of this process has been described in the subsequent section on the methodology of rotational CARS spectroscopy.

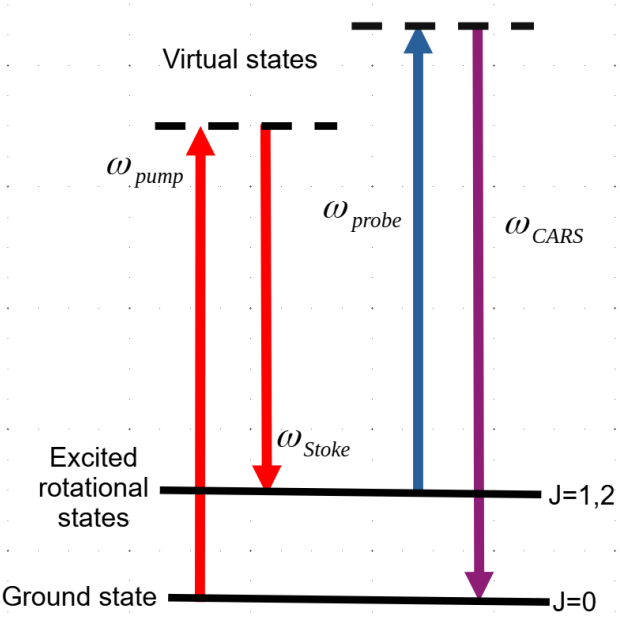

Figure 5.6: Raman shifts for pure rotational CARS spectroscopy showing the behavior of the pump, Stokes, and probe beams that leads to the production of the output CARS signal through the energy transitions exhibited for a representative molecule. Additionally, the selection rules for rotational CARS to occur are also shown in the form of J values besides the corresponding energy state

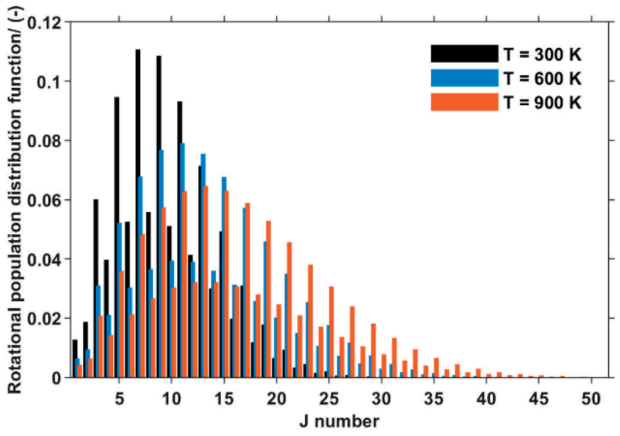

Figure 5.7: Rotational population distribution for N_2 computed at three different temperature cases - 300 K, 600 K, and 900 K - [39]. Note the distinct increase of rotational population states in the higher J number ranges as the temperature is increases from 300 to 900 K

5.3.2. Advantages and disadvantages

The following points summarize the advantages of employing Coherent Anti Stokes-Raman Spectroscopy for analyzing flame front behavior.

- Substantially high spatial resolution (around 20 microns) achievable in comparison to flame front thickness (approximately 0.5 mm)
- Selective detection of specific species of interest possible - Especially useful when performing flame thermometry (detection of nitrogen molecules)
- No requirement for probe volume and receiving apparatus to be in a line-of-sight arrangement.
- Mismatch between repetition rate and laser pulse rate is eliminated by coupling these systems to ensure a single frequency of 1 kHz.
- Capability to probe high-interference environments with little difficulty [38].

However, as with any diagnostic technique, there are some shortcomings that are inherent to CARS as well. These are as follows:

- The instrumentation for performing CARS is substantially more complex in comparison to low-fidelity techniques such as image chemiluminescence.

6

Methodology

6.1. High-speed chemiluminesence

Having explained the fundamentals behind using high-speed flame imagery as a diagnostic approach, the methodology to achieve a viable instrumentation and processing workflow can now be explained. As a start, a simple optical setup based on the fundamental components was constructed as shown in figure 6.7.

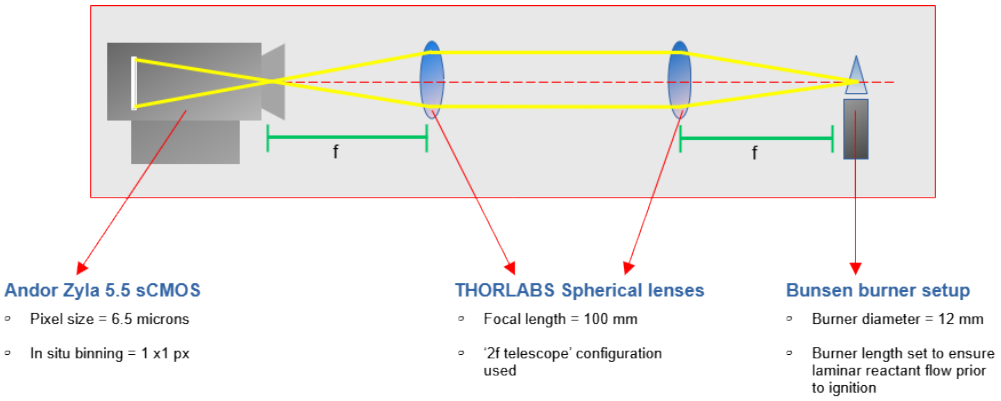

Figure 6.1: Preliminary instrument setup for image processing - The 2f telescopic arrangement has been setup to relay the flame image from the burner to the camera without magnification due to the positioning of the optical elements.

As discussed earlier, a line-of-sight layout with a 2f telescope optical arrangement between the Bunsen flame and the high-speed imaging device was constructed. The high-speed camera chosen was the Andor Zyla 5.5 Megapixel scientific CMOS camera. This imaging device uses a 22 mm sCMOS sensor (measured diagonally) with the ability to achieve a maximum of 1kHz temporal resolution. Specific to our investigation, this camera also involves the use of a global shutter. The global shutter is primarily useful for high-speed applications where the conventional setup of a rolling shutter tends to create motion blur artifacts [40]. In addition to avoiding artifacts, this shutter system also results in lower spatial distortion, higher signal-to-noise ratio, and the capability to work with continuous or pulsed light sources [41]. The 2f-telescope system consists of two THORLABS plano-convex lenses (LA1050-A) of focal length 100 mm that are each placed at a distance of 100 mm (one focal length unit) from either end of the setup as shown in figure 6.1. Between these lenses, an optical relay was created to transmit the light from the flame to the surface of the sensor. It must be noted that these lenses do not produce a magnification of the image since the fundamentals of ray optics ensure that the twin lens system purely acts as a relay. Finally, the burner configuration consists of a 12 mm diameter pipe with its length set to ensure laminar outflow of premixed reactants prior to ignition. With this initial setup, a basic processing algorithm to make use of the flame images was now developed.

6.1.1. Initial attempts at a processing algorithm

With the chemiluminescence optical setup being completed, a preliminary algorithm was sought to be developed to check the quality of the images being generated. With an exposure time set to 0.0199872 seconds, a region of dimensions 1200 x 900 pixels was chosen to encompass the entire inner flame cone. To avoid the possibility of spatial resolution losses, the in-situ binning feature was not employed at this stage. Due to a variety of constraints as explained in section 6.1.5, a sequential acquisition technique was used to capture a larger sample of images (1200 frames) for each flame condition at a temporal resolution of 200 Hz. The objective at this stage was to produce a sufficiently high-contrast, low-noise image of the flame front which could then be employed to extract the frequency of oscillation for a specific flame condition. It must also be noted that knowledge of the obstacles faced during the efforts to extract frequency data were unknown at the time except for the presence of noise and low contrast. Hence, the following overview provides the flow of operations for the most basic algorithm that was attempted.

1. Background noise elimination
2. Intensity normalization
3. Pixel binning

Each of these steps will now be elaborated in detail along with corresponding exemplary results to show their effect on a raw flame image.

1. **Background noise elimination:** Consider the following image frame shown in figure 6.2 extracted from a high-speed sequence of a stochiometric flame captured via the instrument setup shown in figure 6.1. As can be observed, the prevalence of noise in this image is an obstacle to using them for tracking spatial position changes of the flame front. While unavoidable, its presence can be attributed to some specific factors. The biggest contributor among these is the phenomenon of spatial blurring that occurs as a result of high exposure times. This phenomenon is attributed to the fact that the oscillatory frequencies of the flame front and the acquisition rate of the camera are such that the acquisition rate is lower than the oscillatory frequency. This leads to an overlap of multiple flame front positions being recorded within a single image frame. While background elimination of noise will not eliminate this specific artifact problem, a general reduction in the noise present within the image across all regions of the image can still be achieved. This can be achieved by a simple matrix subtraction between each flame image frame and a background image frame. In this case, the background image consists of an unlit burner without changes to the physical setup of the optical instrumentation. By using two-dimensional matrices to represent the two images in terms of their pixel intensities, an element-by-element subtraction generates the following result shown in figure 6.9. However, it must be noted that any noise present within the flame region itself is not addressed by this step.

   The contour of the inner cone of the flame front is now visible in figure 6.3 at a higher contrast compared to figure 6.2. As can also be visually observed in figure 6.3, a substantial reduction in presence of noisy pixels is visible. Quantitatively, the improvement in signal-to-noise ratio can be computed for the raw image and the background noise eliminated image to prove this improvement. By calculating the average of the pixel intensities across the image frame as well as the standard deviation per pixel intensity, a logarithmic value for the signal-to-noise ratio measured in terms of decibels can be found [42]. In the case of figure 6.2, the SN comes out as 5.38 dB. On the other hand, the SN value for an image frame following the background elimination process is computed to be 9.97 dB. While we have taken a random frame from the 1200-frame sample space in each step, the substantial improvement in the quality of the image frame has been proven.
2. **Intensity normalization:** While contrast improvements have been shown to be a by-product of background elimination, this step now deals specifically with the goal of improved contrast and dynamic range. The image frame in figure 6.4 represents the result of performing such normalization on the background eliminated image. To achieve this, the most important quantity is the photon counts per pixel of the image frame. By employing in-built functions available within MATLAB, the pixel with the highest photon count is extracted. Following this, the intensity of all pixels in each image frame is divided by the maximum intensity per frame. As can be seen in figure 6.4, the range of light intensities from the darkest regions surrounding the flame cone to

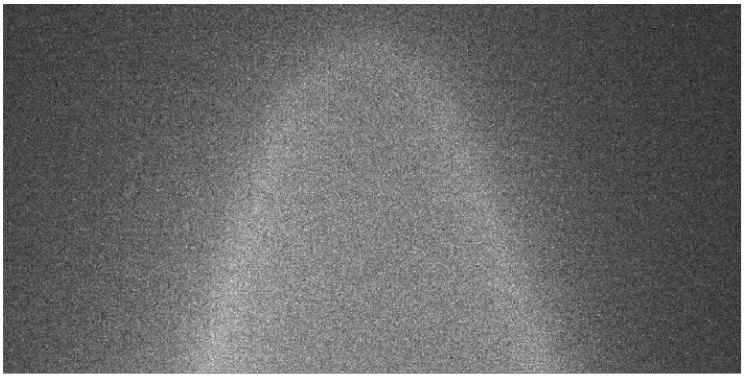

Figure 6.2: Raw flame image prior to processing - This has been derived from the imaging system without prior processing

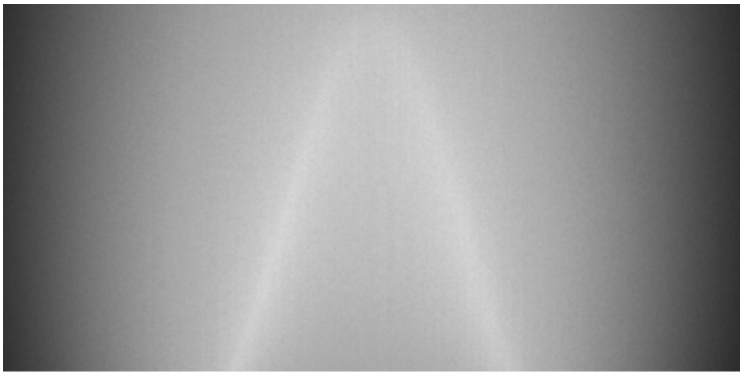

Figure 6.3: Background elimination on the raw flame image. Note the substantial reduction in global noise across the image frame.

the most luminous part has been compressed to numerical values ranging from 0 to 1. Thus, the resulting image is better suited for further processing such as pixel binning as all pixel values have now been normalized. Next, the final step of this preliminary workflow was employed.

3. **Pixel binning:** It is important to note at this stage the order in which these operations are being performed. The definition of binning in this context refers to the aggregation of pixels to generate larger pixel blocks while ensuring the overall size of the image remains the same. Naturally, this process leads to a reduction in the resolution of the image frame. However, the three-dimensional nature of conical flames as opposed to non-conventional flames such as the v-shaped flame and the m-shaped flame makes extracting the inner cone of the flame much more complicated. To this end, a reduction in overall resolution does not help under these circumstances. The following contour plot of the flame image is shown in figure 6.5 following pixel binning. Unlike previous figures portraying the steps of the processing algorithm, contour images have been generated for the purpose of being able to distinguish the inner cone of the flame from the outer region of the flame.

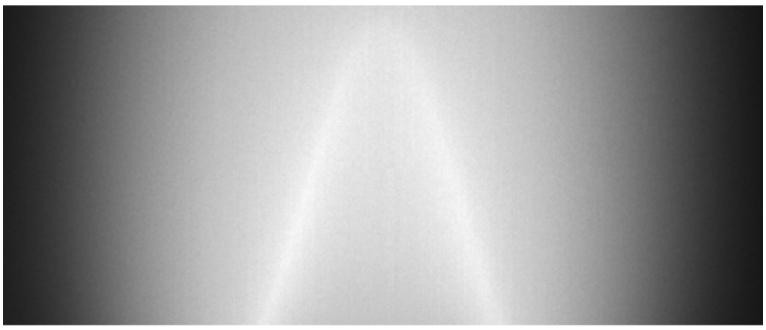

Figure 6.4: Intensity normalized flame image - Performed for computational purposes while preserving image quality

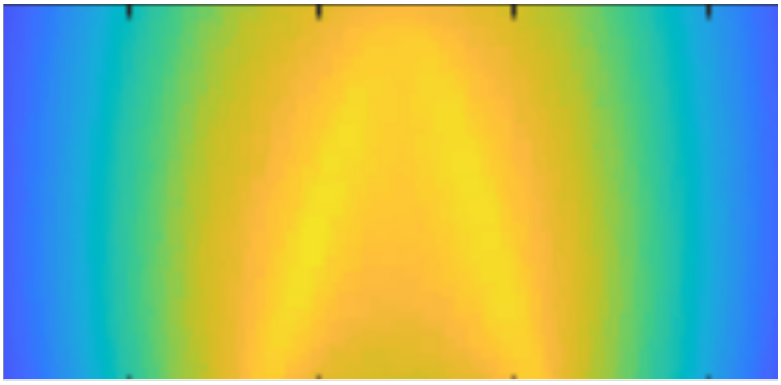

Figure 6.5: Pixel binned flame image frame - Substantial reduction in spatial resolution while increasing the signal-to-noise ratio of the overall image frame

To implement this on an image sequence, a binning 'kernel' of a specified size and shape (measured in terms of the number of pixels) was selected and employed to aggregate image pixels across the frame. By weighting the signal-to-noise ratio against the image resolution, a square kernel of size 4 pixels was chosen. Other possible choices for kernels natively available within MATLAB are also shown along with the chosen approach in figure 6.6. Following kernel selection,

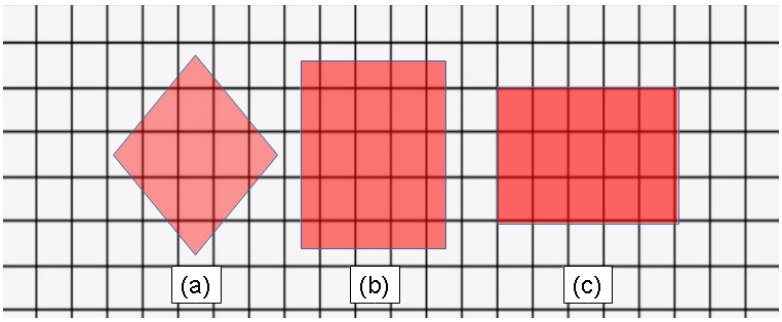

Figure 6.6: Binning kernel shapes – (a) Diamond (b) Square (c) Rectangle. The size of each kernel is shown by the number of pixels that it covers and is not consistent between these three kernel shapes

the resulting output is now shown magnified in figure 6.7 to demonstrate the aggregated pixels or pixel blocks. Additionally, a few select blocks are marked individually to show the larger size and corresponding reduction in image resolution.

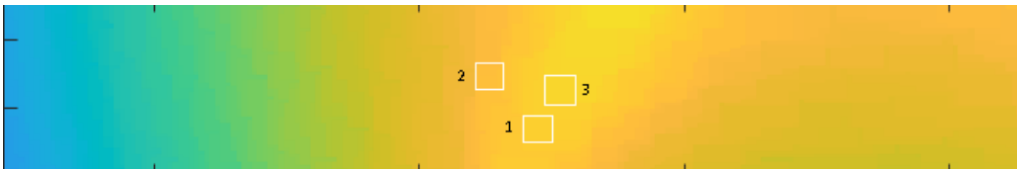

Figure 6.7: Magnified view of post pixel binning with three sample pixel blocks marked. Pixels 1, 2, and 3 roughly fall within the same pixel intensity, and the ability to distinguish between their values is integral to the processing algorithm.

6.1.2. Shortcomings of initial setup and workflow

Having achieved the final result as shown in figures 6.5 and 6.7, there were some obvious improvements as well as major shortcomings that were noticed at this stage. These obstacles are now reviewed. The first and most significant problem of the above setup is the insufficient distinction of the reaction zone from the outer regions of the flame. This is especially troublesome as the algorithm requires the tracking of the exact spatial position of the luminous reaction zone. Next, the improvement in signal-to-noise ratio does not appear to be a positive trade-off in comparison to the loss in overall image resolution. Additionally, the previously mentioned issue of blurring also adds to the problem of resolution loss. This specific issue has to be addressed physically as explained in section 6.7. Finally, the above-mentioned instrument setup shown in figure 6.1 also visually revealed the presence of oscillatory behavior resulting from the ambient conditions around the flame. In other terms, lack of isolation from the surrounding air has been omitted in this preliminary layout.

6.1.3. Modified instrumentation & processing

Based on the shortcomings and obstacles faced with the experimental setup and algorithm, a new modified layout along with changes to the processing workflow was initiated. The representative diagram in figure 6.8 shows these changes along with the new layout. As is visible, the imaging sensor, optics, and burner design have been preserved as they have been. However, the use of a flame shield placed around the Bunsen burner in the shape of a simple cylinder with an exposed opening at the top is a new addition. The dimensions of this shielding cover have been determined such that the flame does not impinge on the shield. Due to the line-of-sight nature of this diagnostics approach, a slit has been provided for this purpose at the appropriate position on the shield.

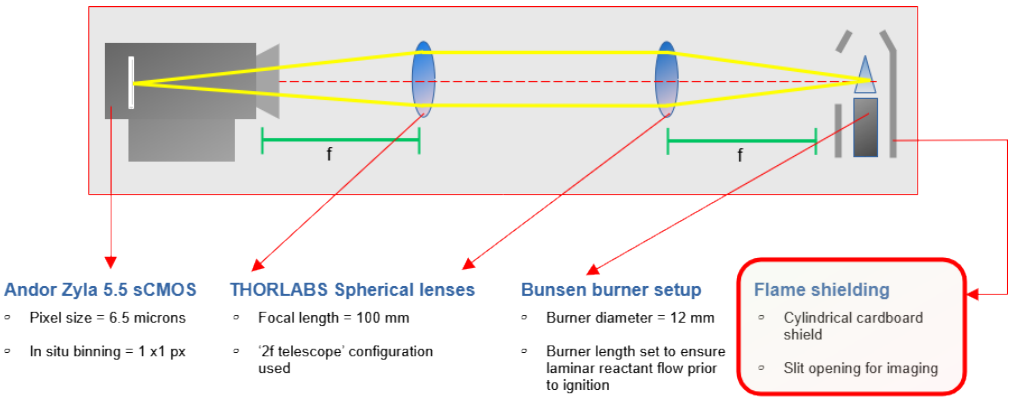

Figure 6.8: Modified experimental layout with modifications indicated. As is visible in the schematic, a simple cardboard shielding was employed to reduce ambient effects on the flame.

6.1.4. An improved algorithm

The following list provides an overview of the new processing workflow attempted to improve the quality of flame datasets that have been captured. It must be noted that these changes include some of the

steps from the preliminary attempt as well as more recent additions to address shortcomings such as the lack of image resolution and problems with discerning the inner cone. The new workflow consists of the following steps:

1. Background noise elimination
2. Intensity normalization
3. Edge detection – High pass filtering
4. Final noise elimination – Low pass filtering

Note here that the steps involving background noise elimination and intensity normalization will not be repeated as these procedures have been described in detail. The major modification in terms of edge detection and noise elimination via mathematical filters will be given greater significance in the following paragraphs.

1. **Edge detection – High pass filtering:** Having eliminated the background noise for each frame of the sequence and normalized the intensity of photon counts, an algorithm for edge detection can be implemented. Consider the example case of a raw image as shown in figure 6.9. If such an image is run through an HPF algorithm, the resulting output is shown in figure 6.10. As can be observed, high-frequency spatial components of the image have become highlighted. This translates to the sharp edge transitions present within the image. Having demonstrated the effectiveness of using this filtering algorithm, the implementation of this step can now be discussed.

Figure 6.9: Example raw image (unprocessed) - [43]. Note the outlines of the human and the camera equipment in the image which form a sharp contrast with the environment in the background.

Mathematically, a high pass filter is defined in its ideal form using the following equation below. The terms u and v refer to the matrix coordinates of the image within the frequency domain. The expression $D(u, v)$ refers to the spatial frequency of a particular pixel coordinate upon which the filter is being applied. Finally, by using a fixed cut-off value D_0 for the spatial frequency, the filter can eliminate certain pixels from the image while enhancing other pixels that fall within the cut-off range.

$$HPF(u, v) = \left[\begin{pmatrix} 0, D(u, v) \leq D_0 \\ 1, D(u, v) > D_0 \end{pmatrix} \right] \tag{6.1}$$

While the equation can be directly applied to a two-dimensional image matrix, there are some practical considerations associated with it. Due to the binary nature of the cut-off value in equation 6.1, images processed through this mathematical filter have been shown to produce ringing artifacts [44]. It must also be considered here that any algorithm implemented must consider the computationally expensive nature of this process as it has to be carried out against each and every pixel in the image frame of each sequence. Thus, to avoid artifacts within the output image,

Figure 6.10: High pass filtered image (processed). The highlighted regions (white) of the image show the sharp edges that are present in the image - [43]

a modified version of the high pass filter equation is now shown in equation 6.2. This form of the HPF is referred to as the Butterworth high-pass filter.

$$HPF(u,v) = \frac{1}{1 + [\frac{D_0}{D(u,v)}]^{2n}} \tag{6.2}$$

As seen within equation 6.2, the terms involved such as D and D_0 have been rearranged such that the cut-off is no longer sharp. In addition to the fractional form of this equation, the exponential quantity $2n$ refers to the order of steepness at which the cut-off takes place. Thus, a reduction of artifacts present within is expected upon using this filter. To better visualize the differences between an ideal filter and a Butterworth filter of a specific order, a plot as shown in figure 6.11 has been generated. Having selected an appropriate filtering expression for edge detection, the

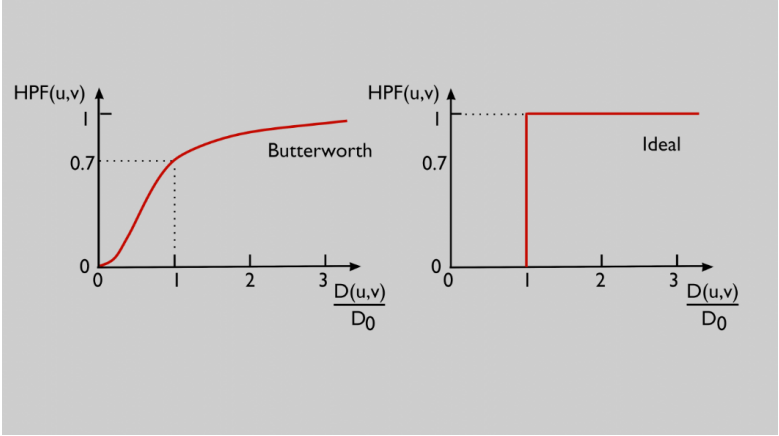

Figure 6.11: Comparison of cut-off behavior between an ideal and Butterworth filter [45]. Note the sharp gradient of the ideal high pass filter (right) is replaced by the gradual cut-off produced by the Butterworth filter (left) which is infinitely configurable in terms of cut-off frequency and slope of the cut-off.

implementation on two-dimensional image matrices can be performed. The mathematical process of convolution is integral to this step. The HPF filter is also converted into a two-dimensional 'kernel matrix for this purpose. A 'kernel' in this process is generated from the multiplication of the unity matrix and the value computed from equation 6.2. Conventionally, such a kernel is limited in terms of matrix dimensions by the size of the matrix to which it is convolved. In this case, the

size of the kernel matrix will be proportional to the quality of the filtered output. Alternatively, the memory requirements and computation time per frame are inversely proportional to the kernel size. Once a trade-off between these two conflicting requirements is made, the actual process of matrix convolution is performed as shown in figure 6.12.

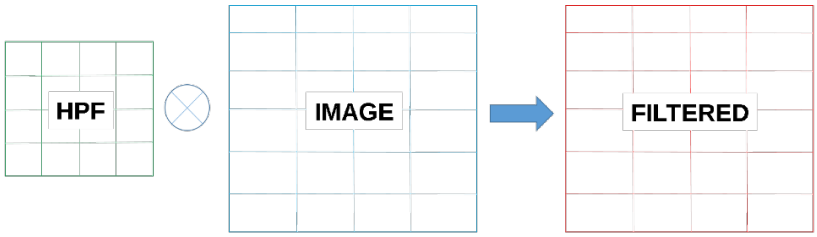

Figure 6.12: Graphical depiction of a convolution between HPF kernel and image matrix. The difference in the size of the HPF matrix and the image matrix has been depicted by their size difference although equal-sized HPF kernels can also be convolved.

While descriptively simple to follow, the exact procedure by which a matrix of photon counts that make up the image is filtered is not straightforward. The use of Fourier transforms plays a key role prior to any convolution process being allowed to take place. This is necessary in order to convert matrix data from the spatial domain (image pixel intensities) to the frequency domain (spatial frequencies). This can also be inferred from the fact that equation 6.2 requires frequency data for comparing against a given cut-off value at each and every pixel coordinate. At this point, it is important to make note that spatial image-based frequencies per frame and the oscillatory frequencies generated from the entire frame sequences are not the same.

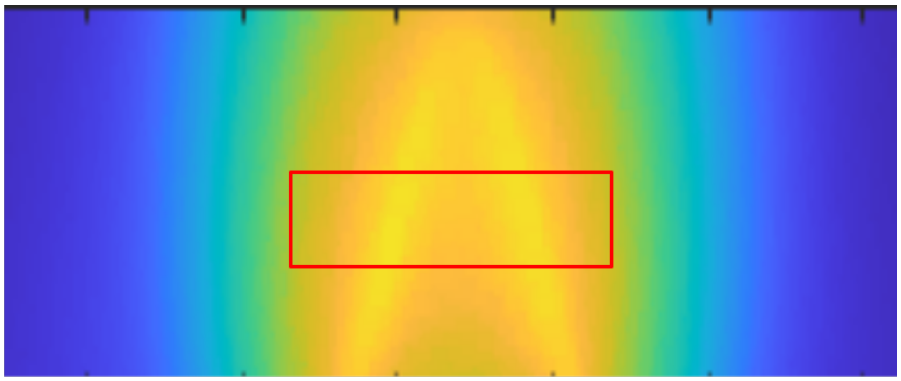

Figure 6.13: Contour plot of flame image post background elimination and intensity normalization. The location of the region that has been magnified in figure 6.14 is now shown in the context of the original image frame.

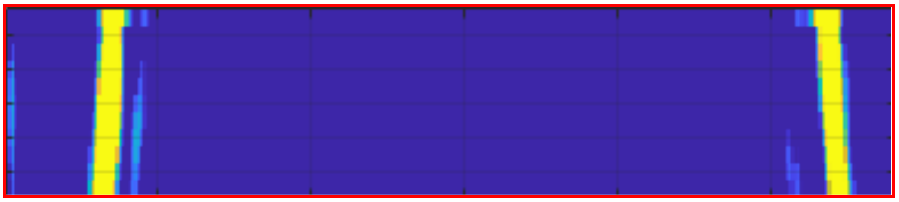

Figure 6.14: Magnified flame image frame post edge detection with visible artifacts. Note that the previous image shown in figure 6.13 is prior to the high-pass filtering process

Having explained the implementation of edge detection, the result of performing this step on a flame image frame can now be demonstrated. Since this step is part of an overall processing workflow, the contour plot of the image frame shown in figure 6.13 shows the result of a flame that has been put through background elimination and intensity normalization. The edge detected

image frame shown in figure 6.14 is especially magnified in order to better visualize the edges of the inner cone of the conical flame that is now made very clearly visible in terms of contrast and dynamic range.

To provide a visual reference, the magnified region from figure 6.14 has also been marked in figure 6.13. In addition to a sharper edge, there are artifacts still present along the direction of the flame branches. These can be attributed to the trial and error process in selecting the filter order n and cut-off frequency D_0. While the intensity of these artifacts is relatively low in comparison to the edge itself, their presence may affect the pixel tracking necessary to record spatial movements of the flame front over time. To this end, the next step in the processing workflow will address this matter.

2. **Final noise elimination – Low pass filtering:** Thus far, the processing pipeline has been successful in extracting the luminous reaction zone while eliminating the outer region of the flame. However, the presence of noise still remains within the core region along with the so-called 'ringing' artifacts are the objective for this final step of the workflow. Before implementation, a brief primer on the filtering technique (low-pass filter) is necessary. In simple terms, the entire procedure can be boiled down to being a form of pixel aggregation. However, instead of a non-weighted averaging for a group of pixel intensity values, the use of distributions of weights is employed. The resulting 'smoothing' effect eliminates any spatial low-frequency noise that is still present within the image. To better demonstrate the effect of these low-pass filters, figure 6.15 shows a side-by-side comparative reduction in noise on a sample image as previously used in the discussion on high-pass filters. In a similar manner to high-pass filters, LPF (low-pass filters) are also classified

Figure 6.15: Effect of applying low-pass filters on an example image. Comparing the unprocessed image on the left, the sharpness of the image has been reduced and an overall blurring effect has been produced.

based on the nature of the distributions employed in performing said aggregation. In this case, the simplest filter using a Gaussian distribution has been chosen. The mathematical form of a Gaussian low pass filter is now shown in equation 6.3.

$$H(u,v) = e^{-D^2(u,v)/2D_0^2} \tag{6.3}$$

As can be seen, some familiar terms appear once again in this expression as well. Unlike the sharp cut-off of the ideal HPF, the fractional terms in equation 6.3 are similar to the expressions seen in the expression for the Butterworth variant of the high-pass filter. Having obtained the expression for the filter, the implementation of the algorithm can now be performed. For this, we once again resort to the process of matrix convolution. The kernel matrix in this case is now made using equation 6.3. To better visualize the kernel, the representative spread of the distribution

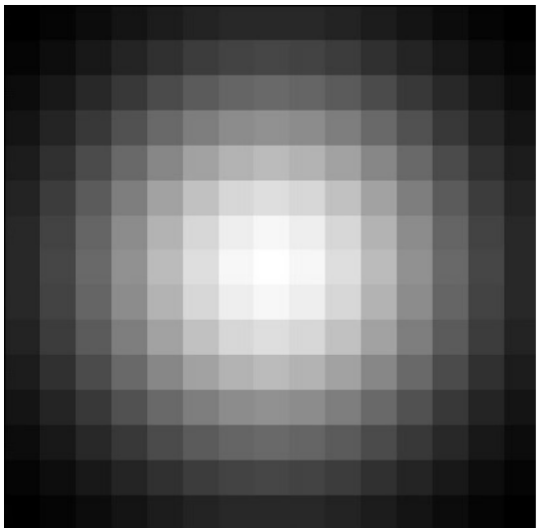

Figure 6.16: Representative Gaussian filter kernel of size 15×15 pixels. The gradient of intensities follows a Gaussian distribution profile in both the x and y-axis.

over some selective pixels is now shown in figure 6.22.

As mentioned prior, the quality of the filtering process (the extent of smoothing) is directly dependent on the size of the kernel being employed for convolving with the image matrix. Note here that the trade-off between improving the signal-to-noise ratio (SN) per frame versus lowering image resolution still exists in this workflow as well. However, the greater control over the noise elimination using the cut-off frequency and size of the kernel favors this approach over the pixel binning technique. In this case, the result of a 6 x6 Gaussian kernel low pass filter can now be seen in figure 6.16. For comparison purposes, it is best to observe figures 6.14 and 6.17 one after another. As is immediately visible, the ringing artifacts present as individual lines are now reduced in intensity and indistinguishable from one another. Additionally, some new striations are visible within the interior of the inner core. While this may appear to hinder the spatial tracking of the flame front, they are sufficiently separated from the luminous reaction zone to be a matter of concern.

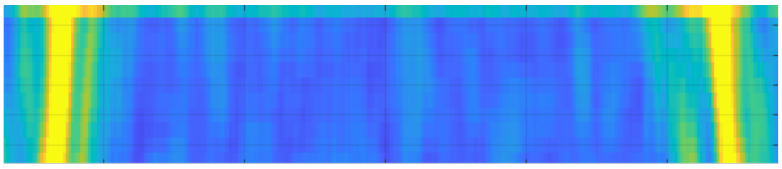

Figure 6.17: Flame front branches post LPF smoothing – Image chemiluminescence. Note that artifacts are still present but are relatively lower in terms of pixel intensities.

6.1.5. Quantifying processed images

Having addressed the shortcomings of the original workflow with the new and improved processing algorithm, the image sequences for the various flame configurations that have been investigated can now be employed to generate oscillation data. This process of generating quantifiable data from high-speed post-processed imagery can now be explained. The primary principle used here can be simply referred to as the ‘target pixel’ tracking approach. To better understand the essence of this method, consider the same flame case that has been employed thus far in understanding the image processing workflow through figures 6.13 to 6.17. For ease of understanding, the final flame image from the preceding section is now repeated with the target region of interest and domain extents highlighted in figure 6.18.

The first step of pixel tracking involves the manual selection of a pixel coordinate within the reaction

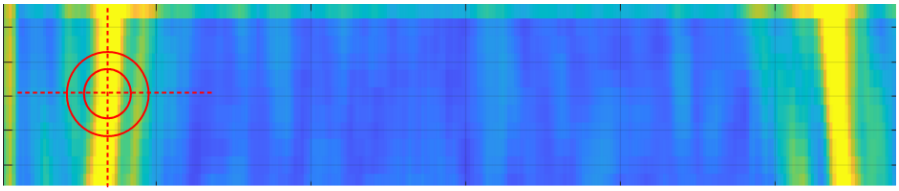

Figure 6.18: Flame image for pixel tracking coordinate selection. The cross-hair shown on the right side branch of the flame depicts the bounds within which the spatial position of the flame-front is recorded.

zone that is viable as a starting point for the algorithm. The center of the cross-hair markings in figure 6.18 is placed in order to depict this target coordinate. While it may appear to be sufficient to track the intensity of the reaction zone at this coordinate, a major limitation is due to the movement of this luminous zone itself. As a result, the chances of the target coordinate not containing the reaction zone are certainly possible. To resolve this problem, all flame images after the first frame of a sequence are tracked using a separate search system. This system makes use of the pixel with the maximum photon counts as a threshold to find the target pixel coordinate of each frame. It must be noted here that the domain of interest in which the pixel with the highest intensity may exist is decided a priori. In this manner, the spatial coordinate of the pixel with the highest intensity is recorded (within the limits of the domain) over the time period of acquiring the sequence. Once a dataset of coordinates is generated over time, they can be visualized in the form of a position-time graph as shown for the above flame configuration in figure 6.19. Specifically, the plot below represents the movement of the target pixel along the x-axis alone.

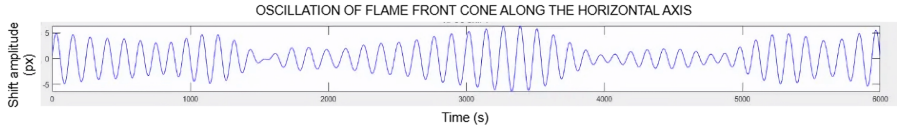

Figure 6.19: Spatial positions of flame-front (target pixel) recorded over a period of time. Within this plot, the amplitude of spatial position shift (in terms of pixels) has been recorded relative to the position recorded during the first frame of the image sequence.

Now, the frequency of oscillations can be extracted from the position data arrays by employing a simple Fourier transformation. In terms of implementation, the Fast Fourier Transform (FFT) algorithm built into the MATLAB library [46] is employed to obtain spectra plots. To visualize the effect of employing this routine on a recorded set of observations, an example signal consisting of oscillatory trends is put through the above-mentioned algorithm to extract the major frequencies present within it. The signal data and the corresponding frequency spectra are shown in figure 6.20. Thus far, the emphasis has been on the manner in which the oscillatory movements of the luminous zone were recorded and converted into their spectral form. However, as can be seen in figure 6.19, only the movement of the flame front along the x-axis (horizontal motion) is demonstrated. The lack of y-axis position data for the reaction zone is due to the inherent limitation of the pixel-tracking approach that has been implemented in the quantification of this phenomenon.

Having set up the image processing and quantification pipeline, the result of performing these steps on a sample flame sequence can be shown. Note that the spectra below in figure 6.21 correspond to the oscillatory data shown in figure 6.19. As is evident, a single peak is generated at a position along the x-axis of the scale that corresponds in this case to a frequency of 5 Hz. At this stage, it is appropriate to elaborate upon a major obstacle that had to be overcome during the initial setup of the imaging system. As is common to any high-speed image-based analysis, there are three interdependent factors to consider when attempting to study a phenomenon [47]. These include the image resolution, the size of the sampled data, and the sampling frequency. In the case of high-speed imaging, the greatest constraining factor is the refresh rate of the sensor placed within the imaging device. However, an experiment-specific problem arises when dealing with oscillations in a flame front. For the experiments conducted in this study, the sCMOS (scientific CMOS) camera is especially useful as its refresh rate

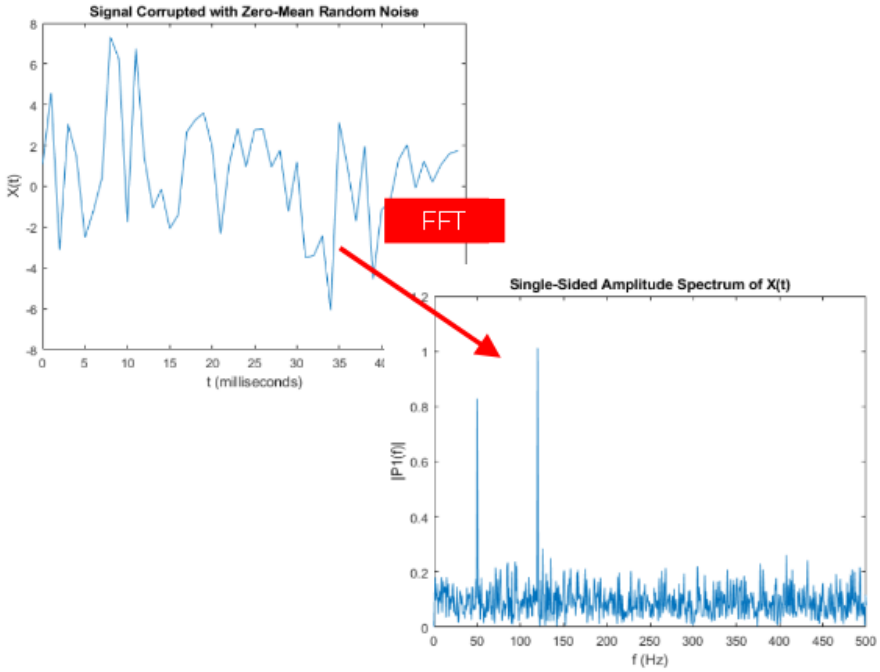

Figure 6.20: FFT implementation on a sample signal showing resulting frequency spectra [46]. This important step in converting spatial position data into frequency data is integral to generating oscillatory data

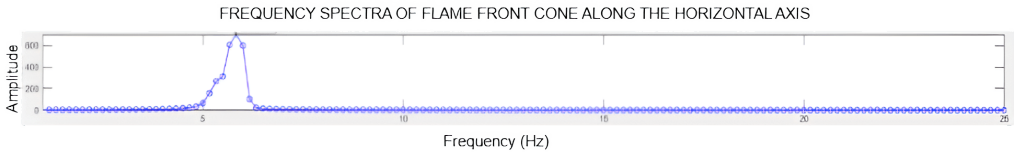

Figure 6.21: Frequency spectra for sample flame configuration. This plot shows the oscillation frequency of 5-6 Hz for the flame configuration shown in figure 6.19.

is primarily limited by the maximum bandwidth of data output possible at any given image resolution [47]. This implies that any increases to the image resolution per frame of a sequence will have a direct penalty on the frequency at which these frames can be acquired. While this may appear as a trivial trade-off, the conflict between choosing a sufficiently high image resolution per frame against selecting an appropriate sampling frequency is not easily solved. This is especially a matter of concern when there is a need is to balance the size of the sample space against the possibility of spatial blurring that can occur with too high an exposure time per frame. Thus, a workaround to resolve this conflict was chosen, thus ensuring the maximum image resolution possible without spatial blurring while simultaneously achieving a high sampling frequency.

Through a process of trial and error, an optimal value of 900×1200 pixels of image resolution per frame and a sampling frequency of 200 Hz was chosen. As is evident from the representative image frame shown in figure 6.22, the images are oriented with a bias toward the y-axis. This has been chosen as opposed to a horizontally biased image resolution (1200×900) due to the change in the size of a laminar premixed flame as it is set to combust at various equivalence ratios throughout the experimental campaign [19]. With these parameters have been set up, the issue of a reduced sample space was addressed through the non-conventional approach of manual batched acquisition. The following schematic shown in figure 6.23 represents the manner in which manual batched acquisition was performed. Due to the limitations of the image acquisition system mentioned earlier, the selection of a specific image resolution implies a strict limitation on the sampling frequency and the size of the sample space for a given time period of acquisition. In the case of the experimental campaign of this study, the physical limit of 200 Hz sampling frequency means a maximum of 400 frames can be acquired within a set time duration. Thus, the crux of this workaround lies in extending the time period of acquisition by

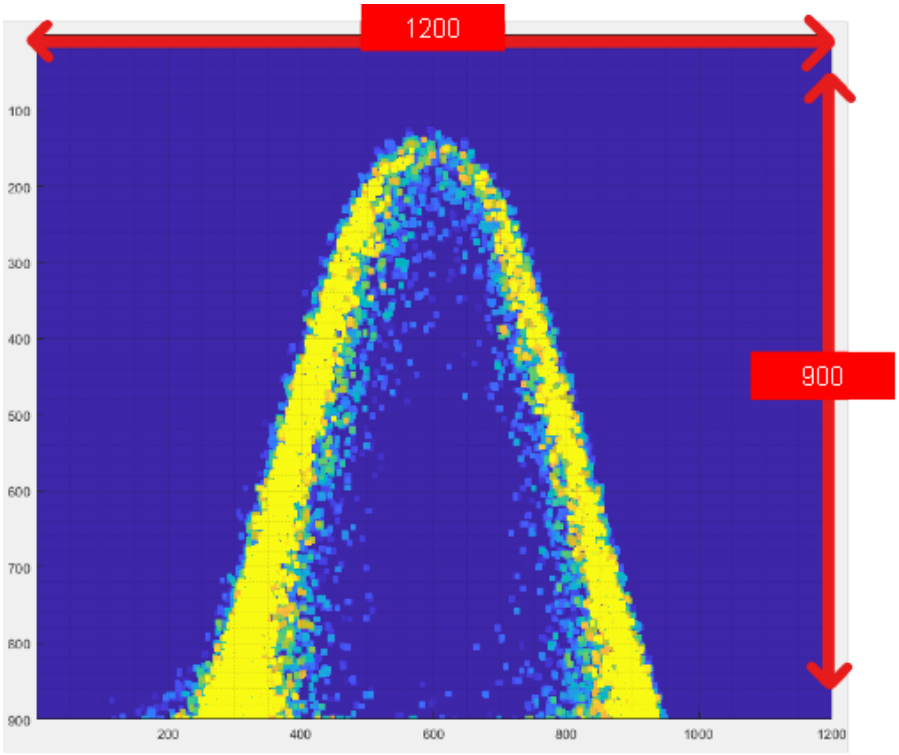

Figure 6.22: Representative image frame for a flame sequence with image resolution highlighted

generating multiple batches of data in a serial order. For all experiments performed during this thesis, three such batches were generated for each flame configuration sequence, thus resulting in a total of 1200 images per sequence. A point of careful consideration in applying this method is to accept that there exists a small time delay between sequences that must be preferably kept as minimal as possible. Due to the low-frequency nature of the phenomenon under investigation, the time delay has not been considered to be of significant concern to the analysis of the results generated.

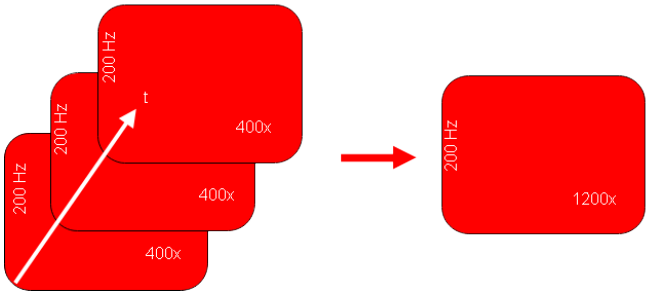

Figure 6.23: Schematic flowchart for the batched acquisition of high-speed imagery - Note that the time delay between each sequence set is considered to be minimal so as to prevent loss of information during these periods.

6.1.6. Spatial resolution of optical setup

The preceding sections have shown that efforts toward addressing the various shortcomings of earlier layouts and workflows have been fruitful. However, the performance of any line-of-sight optical procedure is best understood by knowing the limits of its ability to distinguish two closely spaced objects. In other words, this performance metric refers to the spatial resolution of the optical layout. Additionally, the validity of any analysis performed on the results obtained from this setup is heavily dependent on this parameter.

For determining resolution, the imaging device employed during the experimental campaign has been

reused to ensure consistency in results. The optical setup necessary to perform this involves what is commonly referred to as a 4-f correlator setup. This consists of a two-lens setup placed at a distance corresponding to two focal lengths between them. Additionally, the imaging system and the object being imaged are placed at a distance of one focal length unit away from their respective lenses. In this manner, a '4f' optical relay is generated between the blade edge surface and the imaging device. Under this setup, it is important to note that the image produced at the image plane is of the same magnification as the object. Due to the placement of the two lenses of the same focal length at a distance of '2f' between them, any magnification produced by one lens is nullified by the other. Thus, computations of spatial resolution do not have to consider the magnification factor when dealing with the final output image as produced by the camera. The imaging device is an sCMOS system With a sensor size of 13.5×13.5 mm and a total resolution of 5 megapixels, thus resulting in a pixel size corresponding to a value of 6.5 micrometers. Now, the manner in which this experiment is performed can be explained. In order to generate the kind of image depicted in figure 6.24, a sharp-edged surface is placed with the broad side parallel to the optical path such that it only partially covers the light source. At this point, it must be also noted that the light source employed is a laser source. In this way, when observing through the imaging device, this produces a sharp change in light intensity along the horizontal axis when viewed from left to right. Based on this setup, the edge spread function can be defined as the intensity variation along a specific horizontal axis chosen by the user. A closeup of the chosen coordinates along the horizontal axis is also shown in figure 6.25.

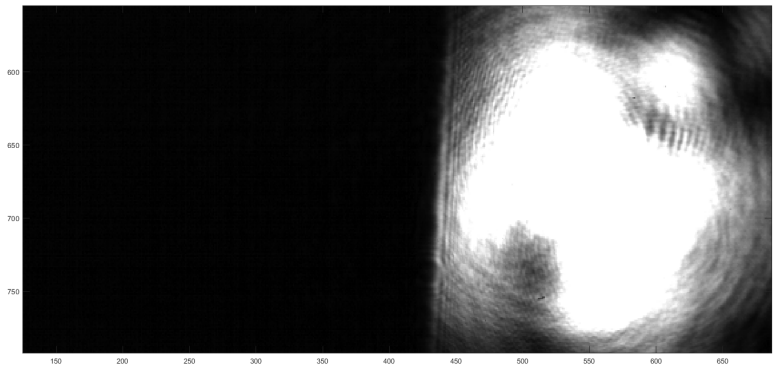

Figure 6.24: Original photo with false coloring to show the light source and blade edge superimposed along the optical path. The dark black region on the left of the image shows the blade surface with the edge intersecting the optical path of the light source.

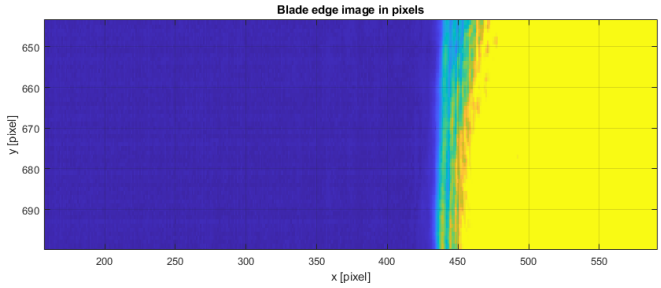

Figure 6.25: Closeup of the horizontal axis showing the drastic change in intensity as we pass from blade surface to light source (left to right). This false-colored contour better depicts the gradients of light intensities from the darkened region to the unobstructed region of the light path.

Following the plotting of the edge spread function, this was then subsequently employed to calculate the line spread function (LSF). Figure 6.26 shows the resulting ESF as plotted against the axis perpendicular to the blade edge. Finally, the FWHM (Full Width Half Maximum) was computed to obtain a spatial resolution for the optical setup of 0.0665 mm or 66.5 microns. In practical terms, this implies that two features in any image generated by this optical setup have to be separated by a minimum of 66.5 microns to be visible as distinct sources during the processing phase.

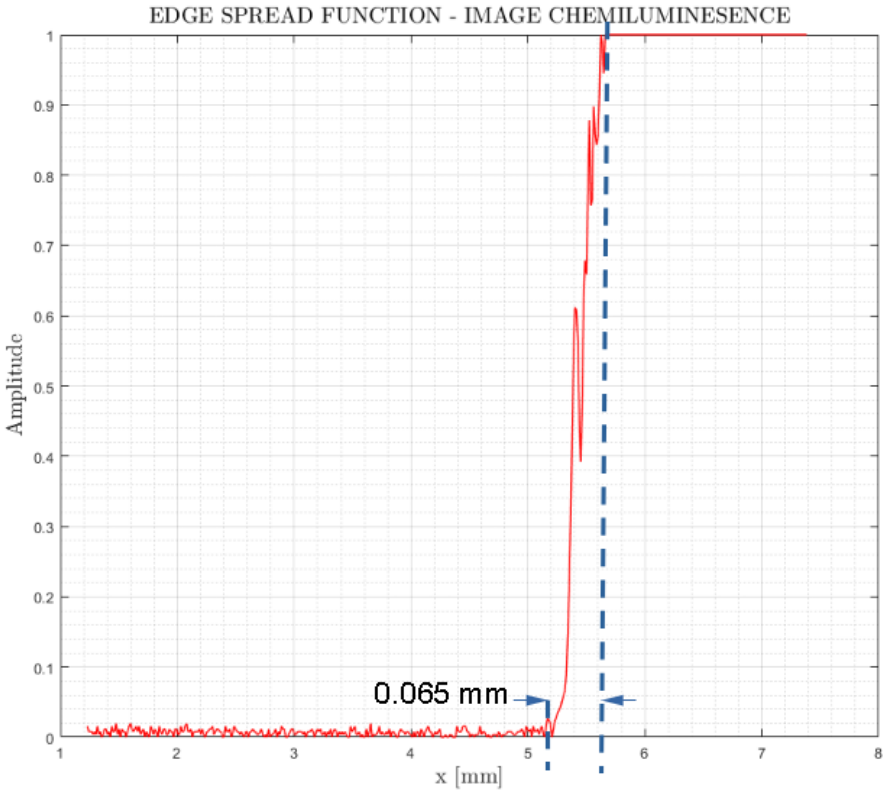

Figure 6.26: Plot of the edge spread function for image chemiluminescence setup at specified horizontal coordinates. The steep slope of the plot indicates the sharp gradient produced by the transition from the obstruction of the blade surface to the unobstructed light path.

6.2. CARS Thermometry

As this investigation only employs this diagnostic method as a secondary technique, the fundamentals of non-linear optics and the exact manner in which the CARS signal is produced have not been elaborated. Instead, the workflow involved in generating temperature data over a period of time from these CARS spectra sequences will be outlined. To extract temperature data from the raw experimental data, a spectral library is generated and used to match with experimental CARS spectra. Such synthetic spectra are created by using a program code that produces spectral data based on the molecular response of specified species for different temperatures and relative concentrations of oxygen molecules in the temporal regime. These responses are then transformed into the corresponding frequency domain by performing Fourier transforms over the temporal dataset, resulting in synthetic CARS spectra. This is now ready to compare with experimental data that has been appropriately processed.

In order to generate such a library that is of sufficient size for performing the analysis, a limit has to be set on the range of temperatures and oxygen concentrations that are expected to be measured during the experiment. Since the experimental campaign involves the generation of methane-air flames, we can use its behavior to understand the above-mentioned temperature and oxygen ranges. Within the ambient surroundings of the flame, the percentages of oxygen and carbon dioxide can be estimated roughly to be 20% oxygen and 0.04% carbon dioxide. On the other extremity, if we consider the case of a stochiometric flame implying that there are sufficient amounts of the oxidizer (in this case oxygen) to allow complete combustion, the oxygen concentration is expected to drop to zero under ideal conditions. Between these two extremities, the use of software code such as CHEM1D that computes changes in oxygen concentrations for various reactant mixtures can be utilized. Using these statistics, the ranges of the theoretical spectra are specified such that temperatures range from 200 to 2500 K and the percentage of oxygen concentration has been set to range between 0 and 0.25.

After the spectral library is created, the experimental spectrum can now be compared to the spec-

tra in the library using a method that involves a spectral fitting technique. This technique requires using the sum of squares of the residuals and a least square interpolation algorithm to find the best match between the above-mentioned datasets. The spectrum with the smallest computed residual will then be used to determine the temperature and concentration corresponding to the observed spectrum. The sum of squares (SSQ) of the residuals is an integral component to perform this step in the analysis workflow. The following equation represents the manner in which the SSQ can be computed when given the experimental and theoretical data.

$$SSQ = \Sigma_i \left[A_i^{theo} - A_I^{exp}\right]^2 \tag{6.4}$$

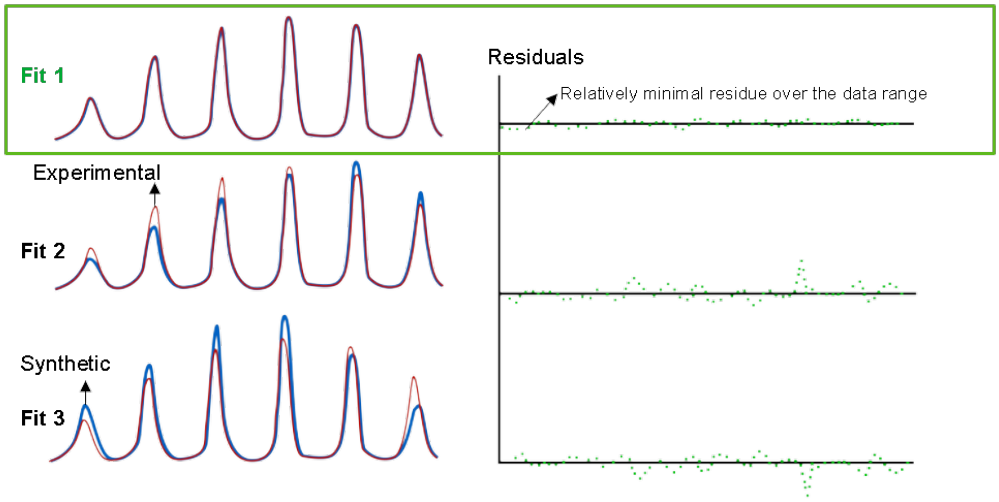

Figure 6.27: Simplified representation of curve fitting and selection of best fit as shown by corresponding residuals for each case. As is visible from the magnitude of the residuals, the selection of a 'best-fit' corresponds to the lowest residuals across the spectral range.

The illustration shown above in figure 6.27 depicts a simple version of the fitting process. By determining the best fit between experimental and theoretically generated data, the accurate temperature and if necessary, the concentrations of a specific species can be determined. Next, a polynomial interpolation method is used to take the nearby fits to interpolate and locate the lowest point of the curve. This minimum point should correspond to the actual measured temperature.

7

Experimental Campaign

Having discussed the diagnostic techniques employed during the analysis, their utilization in exploring the reasons for flame front fluctuation will be the focus here. The experiments that have been conducted in this investigation have been formulated separately based on the two hypotheses that have been proposed. This chapter describes the series of experiments performed for both approaches along with the reasoning behind the manner in which they have been designed.

7.1. Effect of Reynolds number − Parametric study

We shall begin with a recollection of the mathematical model proposed by Cheng [48] as expounded earlier in the chapter on the theory behind the consideration of buoyancy as the core cause of oscillatory behavior. The expression in equation 7.1 restructures the mathematical model shown in the preceding chapters for relating buoyancy forces via density gradients to the frequency of flame front oscillation.

$$\nu = [\frac{0.0018 \cdot u_r^3 \cdot \rho_o \cdot g(\tau^2 + \tau)}{d^2 \mu_o} Re^{2/3}]^{1/4} \tag{7.1}$$

Among the numerous physical quantities such as viscosity, density, and characteristic dimensions, the one parameter that can be easily varied and monitored for any fluid-based experiment is the Reynolds number. Additionally, the use of the Reynolds number also simplifies the expression above as the reactant flow velocity (u_r) can be rewritten to be a function of the Reynolds number itself. Thus, the first set of experiments was designed to affect the frequency of oscillation by directly modifying the Reynolds number of the reactants while ensuring that the flame conditions are kept constant. In the case of the experimental campaign, the equivalence ratio is fixed to a value of 1.2 while the Reynolds number is allowed to vary from 500 to 1000. The decision to select a specific range for the Reynolds number is based on a series of experimental trials. These trials involved checking the duration for which a given flame remained stable under a particular Reynolds number value and a fixed equivalence ratio of 1.2. Within the limits of this thesis, the flame was deemed stable if the blow-out was delayed beyond the acquisition time of the imaging device. The selection of a rich fuel-to-air mixture ($\phi = 1.2$) was made with the intention of ensuring that the flame front generated for the previously mentioned Reynolds number range is sustained throughout the experiment without risking extinguishing of the flame [49].

Specifically, the variation in Reynolds number and thus indirect changes to the flow velocity of the reactants has to be performed such that the mixture ratio is maintained at a constant. As mentioned earlier, the rich fuel-air mixture sustains the flame throughout the regime of Reynolds number settings. While the use of a lean mixture flame with continuous re-ignition of the burner is certainly possible, the high-speed nature of the diagnostic process meant that individual sequences of flame images would be affected by the external disturbance associated with the process of re-ignition on the flame front. As a result, such contributions to the inherent oscillatory frequencies present within the flame cannot be easily eliminated during the post-processing phase. Hence, this preemptive measure to ensure the accuracy of the experiment is a necessary step. Finally, a digital control scheme (Bronkhorst EL-FLOW

SELECT F-201AV/202AV) for this parametric study was chosen to accurately regulate the flow of reactants to the burner. In this way, any possible influence of fluctuations in flow rate is minimized in accordance with the alternative hypothesis proposed at the beginning of this study. Further explanations regarding the various control schemes have been explained in the subsequent sub-section on the second set of experimental campaigns that have been performed following the Reynolds number-based parametric study.

Having worked out the major obstacles to the smooth functioning of this experimental set, the flame configurations to be investigated were chosen. The first and most important configuration is that of the standard conical flame. The conventional design of the burner and substantial database of its characteristics lead to the reasoning that the effect of buoyancy can be observed with all other properties well accounted for. The primary challenge in the case of observing these low-frequency fluctuations for such a flame configuration is the overlapping nature of the information slices acquired by the imaging device. To better explain this problem, the schematic in figure 7.1 depicts a single image frame in the process of acquisition by the image chemiluminescence setup. The conical flame is its subject of interest and the numerous data planes that may overlap with one another are also depicted. Following

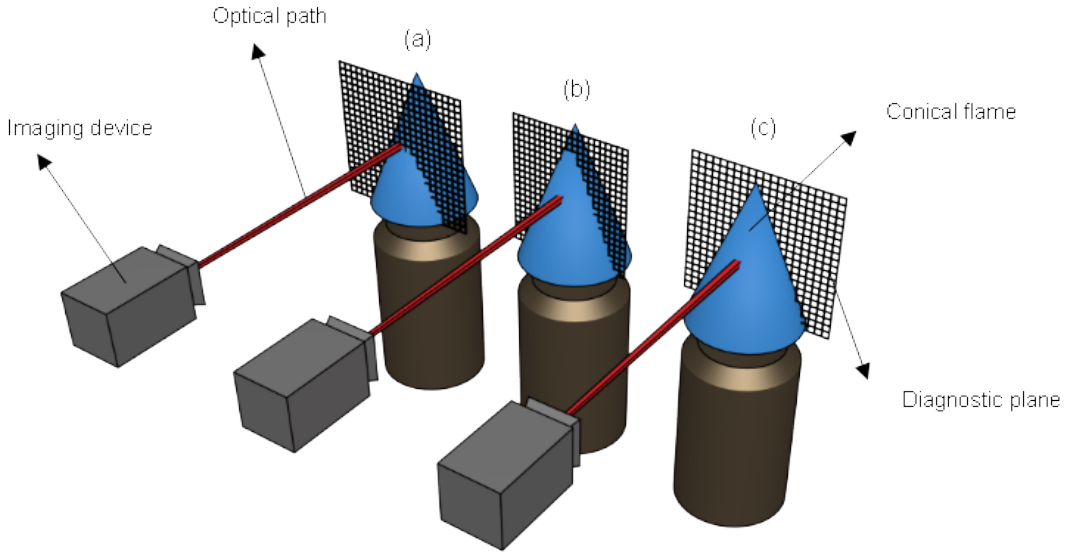

Figure 7.1: Overlap of multiple data planes within a conical flame for line of sight optical diagnostics – Possible diagnostic slices shown as (a),(b) and (c) will then overlap with each other when the image frame is captured.

the conical flame, the next experiment was set up using a v-shaped flame with all other components of the experimental setup left intact. Unlike the well-studied characteristics of the bunsen flame, the two-dimensional v-shaped flame has been chosen for purely bench-marking purposes. This decision was made based on the inherent stability and non-overlapping nature of such a flame. To gain a better understanding of such a configuration, the schematic shown in figure 7.2 represents the manner in which a conventional burner has been modified to produce v-shaped flames. As can be observed, the placement of a cylindrical rod at the center of the burner outlet generates two branches from a common junction in a v-shaped formation.

However, the axisymmetric nature of conical flames is not observed in this case. Instead, the two flame branches (sheets) generated here are symmetrical. Naturally, this completely negates the multiple diagnostic planes that may occur and the resulting mix of image data. As described earlier, a similar series of datasets for a fixed equivalence ratio of 1.2 and a range of Reynolds numbers from 500 to 1000 were acquired. With all other parts of the experimental setup remaining the same, the ease of employing a v-shaped flame to obtain frequency data was clearly evident when performing these extractions.

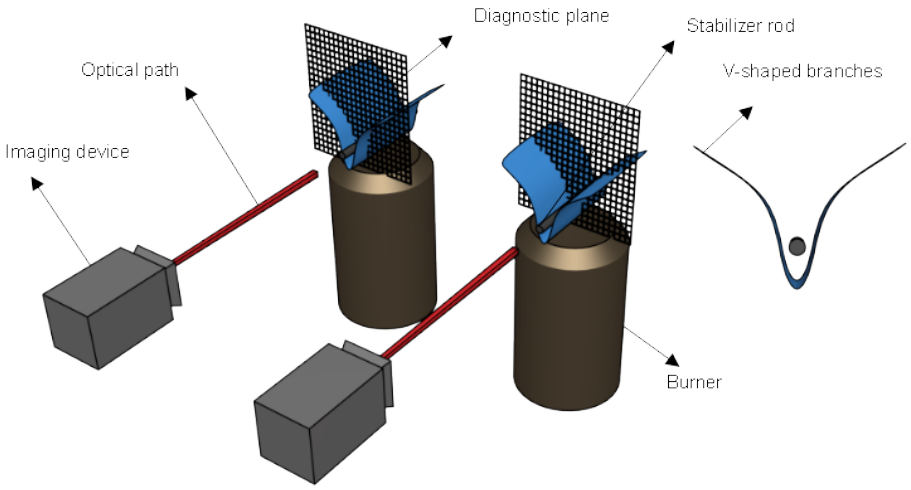

Figure 7.2: V-shaped flame setup for conventional burner using stabilizer rod – Lack of overlap due to shape of flame front shown via multiple diagnostic planes

Finally, the third set of experiments within the parametric study phase of the campaign is a special test case involving an unconventional flame configuration. This configuration involves the inversion of the conical flame burner such that the direction of the flame cone is aligned with the force of gravity. The main impetus behind performing a Reynolds number-based analysis on an inverted flame is to produce a control dataset against conventional conical flame data. However, some interesting visual behavior unique to the inverted flame was observed. The following image in figure 7.3 shows a sequence of Reynolds number cases at 500, 700, and 1000 and the accompanying change in flame front shape. An example of a raw image captured using image chemiluminescence for an inverted flame burner is

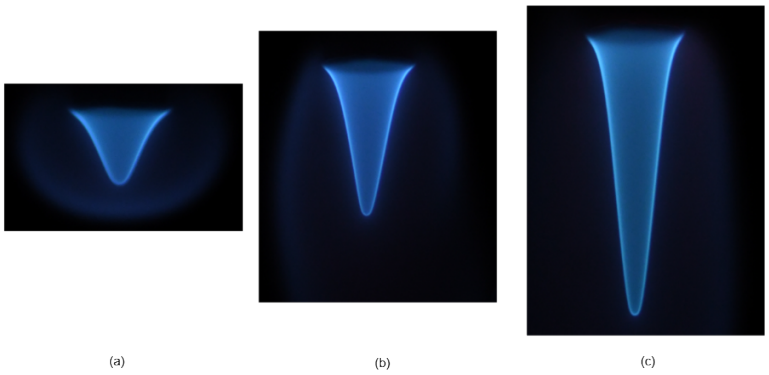

Figure 7.3: Shape changes observed in the inverted conical flame front when varying the Re value from 500 (a), 700 (b), and 1000 (c) at $\phi = 1.2$. As the Reynolds number is increased, the spherical outer region transforms into a distorted ellipse.

shown in figure 7.4 for a visual demonstration of its physical characteristics.

As can be seen from the figure above, a unique feature pertaining to such a flame is the spherical curvature of the outer region of the flame. A direct reason behind this phenomenon is the interaction that is occurring between the opposing forces of gravity and the inherent nature of a flame front to align itself along the direction of the density gradients present in its ambient surroundings. Thus, the self-righting nature of the flame cone is always a matter of concern when such a flame is set up and allowed to burn over a period of time. To expand on this issue, the risks involved in employing premixed flames in any burner have to be mentioned. As is obvious, the concept of a premixed flame implies that the fuel and air in preset quantities are mixed prior to ignition. Hence, the reactant mixture present even

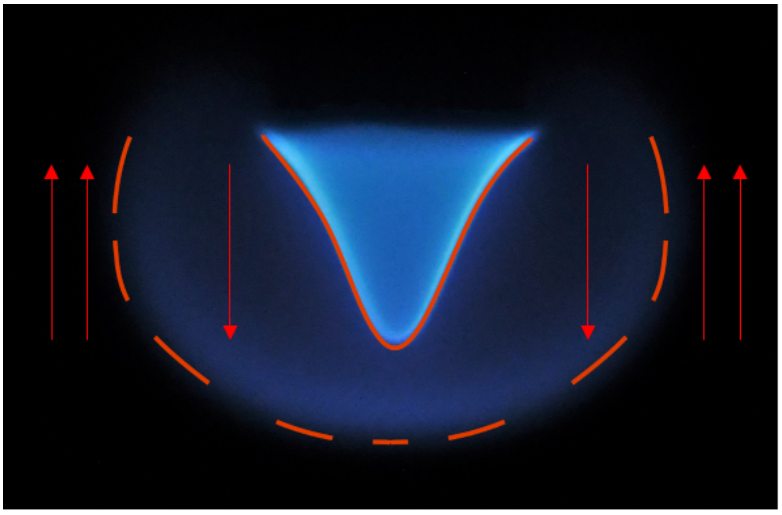

Figure 7.4: Inverted conical flame with the spherical outer region – Direction of density gradients and reactant flow marked using arrows. The opposition between the density gradients and reactant flow vectors is key to generating the characteristics low Re spherical shape.

prior to the exit of the burner outlet is readily combustible. Under these circumstances, the possibility of blowback is a likely event. Furthermore, this problem is enhanced when the entire burner setup is inverted. The following image in figure 7.5 captured in the instance prior to a possible blow-back event shows the nature of this problem.

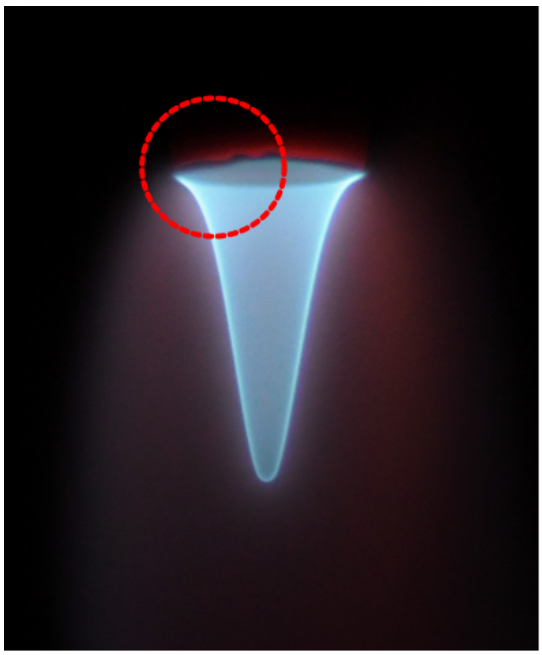

Figure 7.5: Heating of burner lip (indicated in red) prior to blow-back for an inverted methane-air premixed flame. If sustained, distortion of the burner lip is also an issue in addition to the flame blow-back.

As is made visible at the burner lip, the tendency to heat the metal edge of the burner is a lot higher due to the inversion process. Without the presence of a cooling system, such a setup risks the failure of the burner pipe. Therefore, the experimental campaign for recording observations of the inverted burner was performed while paying attention to the health of the burner prior to and post each session of ignition. In this way, each case of Reynolds number between 500-1000 at a fixed equivalence ratio

of 1.2 was extracted with sufficient intervals provided between the high-speed acquisitions for cooling of the burner lip and the prevention of blow-back risks.

7.2. Effect of heat release ratio – Parametric study

Another variable of interest observable in the mathematical model shown in equation 6.1 is the heat release ratio. As described within the theoretical description of the model, this term describes the ratio of the flame-front temperature to that of the reactants. The evaluation of this variable by Kostiuk and Cheng [48] has been performed by using the heat release ratio as a normalizing parameter against the frequency of oscillation. However, the need for this second set of experiments comes from the manner in which the normalization was originally performed using a theoretical adiabatic flame temperature [50] as opposed to in-situ experimental data. To address this possibility, the use of a high-accuracy CARS spectroscopy to extract temperature data was selected. The details of the manner in which this instrumental setup has been used have been explained within the previous chapter. Since this phase of the experimental campaign is a parametric study, the temperature data of the flame at a fixed spatial position has been extracted at flow conditions that match the parametric studies performed using Reynolds number (Re). By doing so, it was expected that the temperature data obtained at a particular flow condition can then be used to normalize frequency data for the range of Re = 500-1000. In this manner, the effect of the heat release ratio on the frequency of oscillation for the flame front can be evaluated in an experimental manner. Specifically, the correlation between flow conditions (Re) and normalized frequency (also referred to as reduced pulsation frequency) is of interest in performing these experiments.

7.3. Effect of flow rate fluctuation – Assessing control schemes

Having performed the two phases of experiments for investigating the buoyancy hypothesis, the alternative proposal of flow rate fluctuations being the underlying cause of low-frequency oscillations was addressed. To this effect, the experiments necessary for assessing this line of reasoning have been designed based on the manner in which the reactants of a laminar premixed flame are metered to the burner outlet. Specifically, two schemes based on the accuracy of maintaining a set value of flow rates for the reactant have been made the criteria. On a broad basis, this leads to two categories of control methods – analog flow control and digital flow control setups.

The analog control system is represented here by a mechanical float valve rotameter and the digital control equipment (Bronkhorst EL-FLOW SELECT F-201AV/202AV) are both shown in figure 7.6. Since this part of the campaign involves the evaluation of flow rate fluctuation as a possible cause, other contributing factors that may affect oscillatory behavior have to be controlled. To achieve this, the flow conditions in the form of the Reynolds number have been fixed at a constant value of 700 throughout this second phase of experimentation. This value has been chosen by a process of various trials conducted for values of Reynolds number between 500 and 1000. Using the quality of the raw image data obtained within these trial datasets, the nominal value of Re=500 was finalized. An additional reason for selecting a lower Reynolds number is to ensure that the flame remains ignited across the spectrum of reactant mixtures. Next, the flame conditions were set in the form of a range of equivalence ratios from lean to rich mixtures. The decision to generate data over a wide range of reactant mixtures is based on a comparative study into the effects of equivalence ratio on a standard conical flame as conducted by Krikunova [16].

The specific values of equivalence ratios chosen to range from 0.9 to 1.4. While leaner mixtures below 0.9 are physically possible, the reference data for behavior of frequency against mixture ratio is biased towards stoichiometric and richer mixtures [14]. Having finalized the parameters of this phase of the campaign, the flame configurations were also selected at this stage. The first and foremost case is that of the standard conical flame followed by benchmark tests using a v-shaped flame. Thus, the overall set of experiments involves two types of tests for each flame configuration with alternative control schemes.

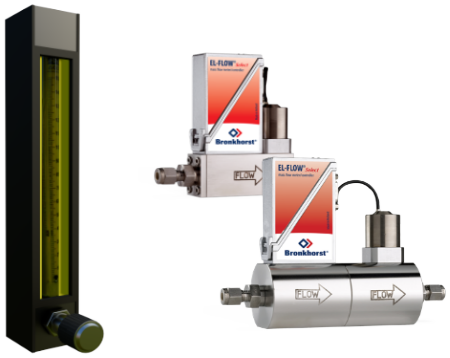

Figure 7.6: Mechanical valve rotameters (left) and digital flow controller (right) as employed for assessing effects of flow rate fluctuations. With the lack of a feedback control system for the analog flow controllers, an inbuilt handicap in terms of accuracy is expected.

8

Results and Discussions

Having performed a wide range of experiments aimed at shedding light upon the two main proposed hypotheses, the outcomes of these investigations can now be examined in this chapter along with further campaigns as deemed necessary. It must be noted at this stage that the results of the experiments have been split into two sections. The first section focuses on the parametric study of the mathematical model as described in equation 6.1 wherein the Reynolds number and heat release ratio were individually evaluated. Within this, the effect of varying the flame shapes has also been compared and contrasted to extract some indications by which the concept of buoyancy as a significant cause can be expounded. Alternatively, the subsequent section discusses the effects of alternative control schemes in an effort to make flow rate fluctuation a contributing factor toward the low-frequency oscillatory behavior of flame fronts.

8.1. Effects of flow rate fluctuations

Prior to discussing the outcomes of the parametric study, the possibility of variations in the flow rate of reactants being supplied to the burner has to be clarified. To this end, the image data extracted for the standard conical flame for a fixed range of equivalence ratios (0.9-1.4) have been plotted in terms of the respective oscillation frequencies under constant flow conditions (Re=500). It must be noted at this stage that the primary emphasis for examining flow rate fluctuation is the conventional conical methane-air flame as opposed to the wide variety of flame shapes that have been tested for benchmarking purposes. Hence, the first observable trend in the form of figure 8.1 represents the comparative effects of employing digital flow control (Bronkhorst EL-FLOW SELECT F-201AV/202AV series) against a mechanical float valve rotameter setup.

The first and foremost observation from this comparison in figure 8.1 is the substantial decrease in oscillation frequency ranging from 22% to 25% that has resulted from the use of a digital control scheme. We can attribute this reduction purely to the method of flow control due to the measures taken to maintain constant flow conditions across the range of equivalence ratios. Next, the overall manner in which these frequencies are distributed over the range of equivalence ratios is also a matter of interest. While the previously noted reduction has occurred, the effect of the equivalence ratio on the oscillatory behavior remains unaffected. This trend across various fuel-oxidizer mixtures is in close agreement with the behavior of high Reynolds number (Re>1250) conical flames as studied by Krikunova [16]. It must be noted at this stage that an order of magnitude reduction in uncertainty of the measured flow rate is now possible with a digital flow control setup.

Despite this greater degree of individual control over the fuel and oxidizer, the oscillatory effect is not completely eliminated. Additionally, the unchanged trend with an equivalence ratio is greater proof that other factors are also at play in maintaining this trend. Hence, the phenomenon of flow rate fluctuation by itself cannot be considered a core cause giving rise to low-frequency oscillations within the flame front. However, this does not rule out the phenomenon completely. The significant reduction of up to 25 % is indicative of the possibility of constructing improved burner designs in combination with precise

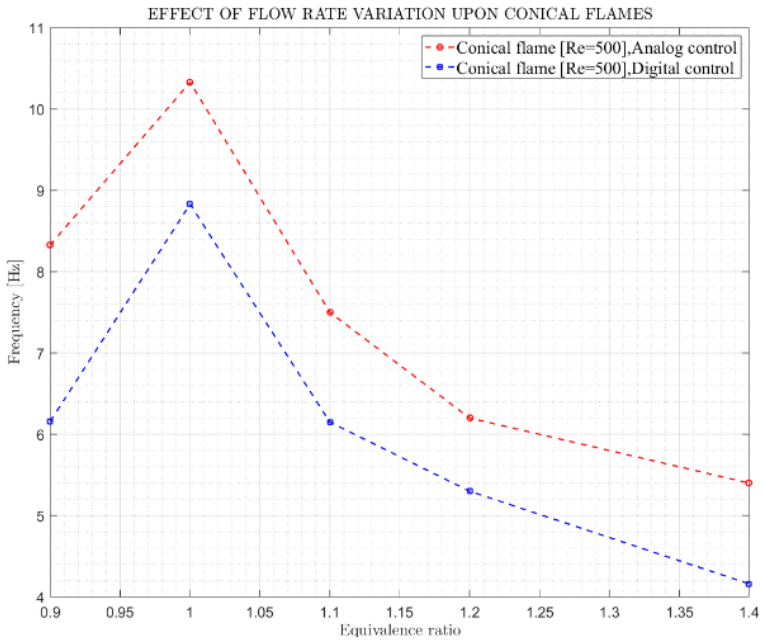

Figure 8.1: Oscillation frequency versus equivalence ratio for differing control schemes for constant flow conditions for a conical-shaped flame. Apart from the relatively constant separation in oscillation frequencies, the overall trend has remained constant between the two control schemes.

digital flow control to minimize the contribution of flow rate fluctuation to low-frequency oscillations. This is explored in greater detail within the subsequent chapter on the mitigation efforts conducted based on the lessons learned from the preceding experimental campaign.

8.2. Effects of buoyancy – Parametric studies

Having established the possibility of the simpler hypothesis of flow rate fluctuation as a core cause, the phenomenon-based hypothesis of buoyancy forces affecting the flame front can now be understood from the parametric study that has been performed. Beginning with the first parameter of the Reynolds number, the experimental campaign, in this case, consisted of varying the Re values (Re=500-1000) within a set range while keeping the properties of the flame front constant ($\phi = 1.2$). Due to the wide range of flame configurations that have been tested for a range of Re values, greater freedom is available regarding performing comparative studies. One such comparison is shown in figure 8.2 wherein the effect of varying the Reynolds number for a conical flame and an inverted flame has been recorded for a constant fuel-oxidizer mixture. In this way, a primary way to verify the mathematical model shown in equation 6.1 is verified in terms of flow conditions.

While the inverted flame burner is the most unique case tested amongst flame configurations employed within this study, a direct comparison between such a flame and the standard conical flame reveals some differences that are of interest. Unlike the results of varying the control scheme of the experiment, the effect of changing the Reynolds number generates a more varied response in terms of oscillation frequency between the two flame configurations (conical and inverted). Clearly, the inverted flame exhibits a significant reduction in oscillation frequency ranging from a minimum of 17% to a maximum of 21% especially as the Reynolds number is progressively increased. On the other hand, the behavior of the conical flame burner in response to varying the Re value is non-linear as expected. This is in agreement with the experimental analysis performed by Cheng [14] for a premixed laminar flame front.

Returning to the behavior of the inverted flame, the progressive suppression of the oscillation frequency also exhibits significantly higher non-linearity in comparison to the conical flame. A possible explanation is the introduction of new contributing factors in replacement for the minimized effects of buoyancy

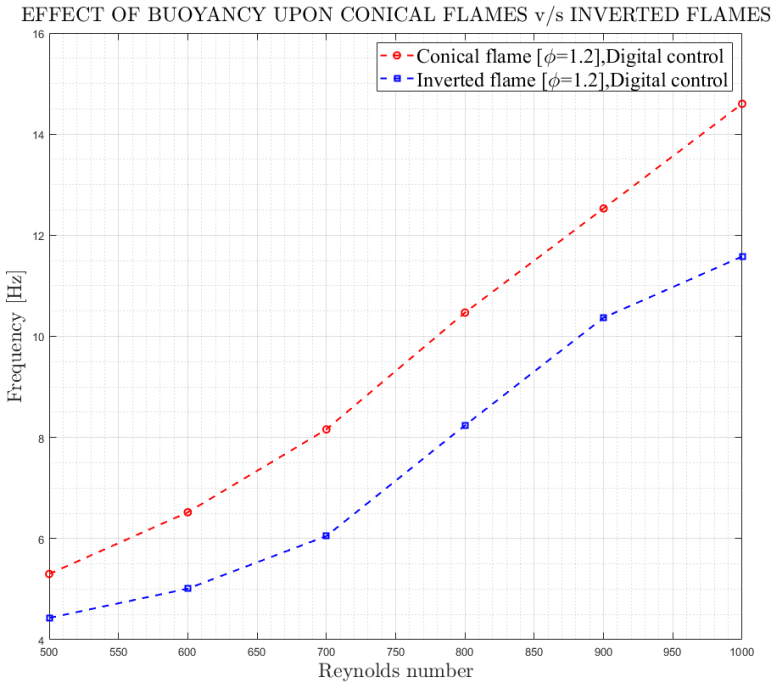

Figure 8.2: Oscillation frequency versus Reynolds number at a constant equivalence ratio for a standard conical flame and an inverted flame burner. The loss of the tendency to maintain linearity in the case of the inverted flame is evident.

as explained in the previous chapter. More precisely, these new contributing factors may not be unique to this flame configuration. Instead, the suppression of two core factors of buoyancy and flow rate fluctuation has now brought these smaller contributors to the forefront. One such cause can be attributed to the presence of ambient air gradients that have not been completely eliminated from the flame surroundings. While the chapter describing the diagnostic setup stated the presence of a physical air shield surrounding the flame, this was eliminated for the inverted flame after repeated difficulties with addressing the risks of the inverted burner setup. Once again, the reduction in oscillation frequency exhibits the possibility of adapting such inverted burners as a possible solution for mitigating low-scale frequency oscillations. While not applicable to every situation wherein such minimization of oscillation is required due to the inherent problems with the burner design, niche cases may exist for such a burner to be utilized. However, a more practical solution that utilizes the lessons learned from these observations along with the bench-marking studies performed using the standard conical flame is required if mitigation or substantial minimization of low-scale oscillatory behavior is to be realized.

Having explored the effect of Reynolds number as an indirect parameter in the control of buoyancy forces, another factor that has been considered during this study is the heat release ratio. As explained in the previous chapter, the numerical model that has been employed as the starting point for these investigations consists of multiple variables that influence the oscillatory frequencies of the flame front. Among these, the heat release ratio is the other variable that can now be examined. As explained in the section on the methodology of CARS thermometry, the extraction of temperature data is performed through a process of curve fitting experimental data to a library of molecular spectra. However, since this is a temporal analysis of temperature data, some form of statistical analysis is necessary prior to obtaining a single temperature value for a given flame configuration. With such datasets, an evaluation of the quality of the dataset can be made by observing the mean as well as the standard deviation of the specific dataset. While the standard deviation is a good way to assess the spread of temperature data over the acquisition period, a more detailed representation can be generated by fitting a probability density functions (PDF) which in this case is a normal distribution function over the histogram of each data point of the sample space [51]. This is especially integral to large datasets as it allows for the discerning of patterns that are unique to the phenomenon involved. While the above mentioned

statistical analysis has been carried out for each dataset case employed during CARS thermometry, an example of the PDF along with the statistical measures such as the mean and standard deviation for the temperature data acquired for a stochiometric methane-air flame is now shown below in figure 8.3. At this point, it must be clearly mentioned that the thermometry analysis has been conducted at multiple points in the vicinity of the flame-front. These points were chosen to allow for the selection of a dataset from among these points that best matches the theoretical temperature data (adiabatic flame temperature).A visual representation of these point measurement locations set at 0.5 cm intervals from the outer cone of the flame to the center of the inner cone have been shown in figure 8.3.

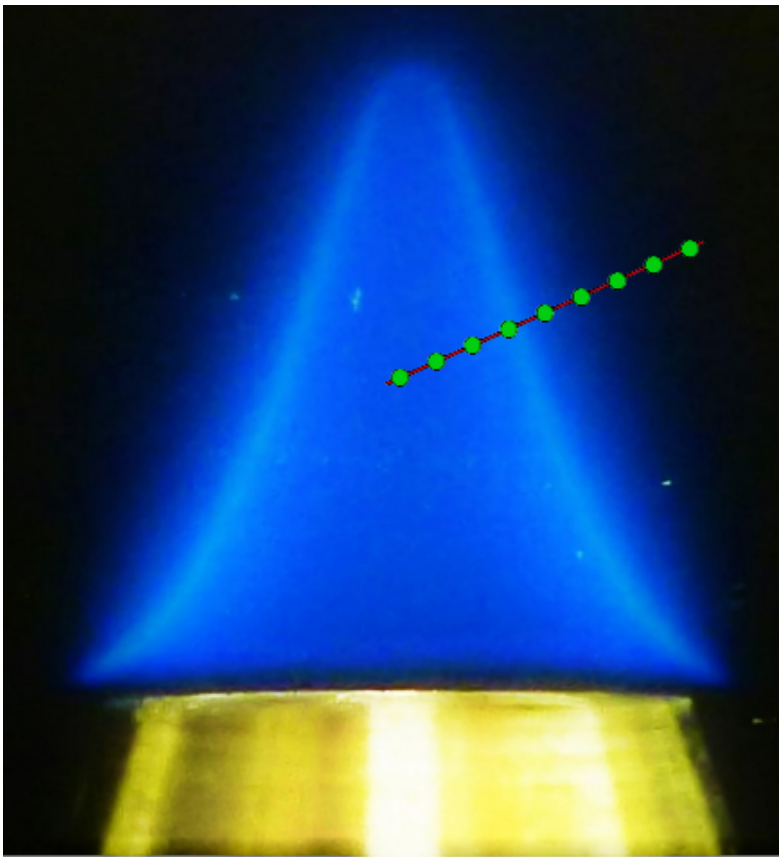

Figure 8.3: Representation of point measurement locations for CARS thermometry on the methane-air premixed flame - The green spots represent the diagnostic points with the red line indicating the axis along which these measurements have been made

As can be seen from the plot above in figure 8.4, a mean temperature of 2020.2 K is achieved for the dataset when employing a stochiometric flame at a position within the flame-front. We can confirm the accuracy of this measurement by comparing it with the adiabatic flame temperature data for the same fuel-air mixture. Additionally, since the adiabatic temperature does not vary with the Reynolds number, the results from the experimental campaign when attempting to evaluate the effect of heat release ratio on oscillatory phenomena have all been checked with theoretical values for the adiabatic flame temperature. For example, the following plot in figure 8.5 shows the adiabatic flame temperature for various equivalence ratios as measured by the investigations by Janto [52]. If we now compare the mean temperature as indicated within figure 8.4 taking into consideration the standard deviation, the CARS temperature measurement is well within the theoretical value that would be expected at the stochiometric ratio for a methane-air premixed flame.

Having established the validity of the individual temperature data-points that have been generated from the CARS spectra dataset, the results of the analysis of the heat release ratio as a controlling parameter towards oscillatory phenomenon can now be explored. This has been portrayed by a normalized frequency plot against the Reynolds number for a fixed equivalence ratio and is explained in greater de-

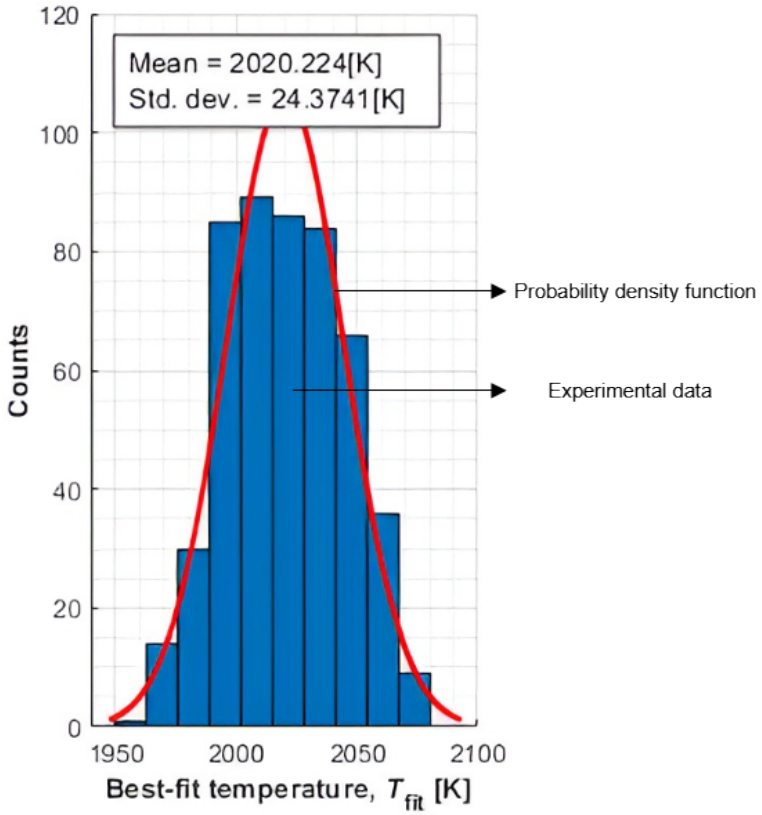

Figure 8.4: Probability density function fitted over histogram of temperature data points for a stochiometric methane-air flame at a fixed point within the flame-front region. While deviating by 24.37 K, the mean value offers a data point in the normalization process carried out.

tail in the following paragraph. The following plot shown in figure 8.6 represents normalized frequency data for a standard conical flame against the variation in Reynolds number. The difference between the data shown in figure 8.6 versus the frequency data plotted in figure 8.2 is in the above-mentioned process of normalization that has been carried out at each data point.

Here, the normalization process has been carried out using the heat release ratio as the factor for all frequency data. This part of the experimental campaign was performed based on the theoretical calculations generated by Cheng et al [14] using the adiabatic flame temperature based on flame conditions as the input for computing the heat release ratio. Using high-accuracy CARS spectroscopy, an experimental analog of the same process has been carried out. To refresh the memory of the reader, the heat release ratio is computed as shown in equation 7.1.

$$\tau = [\frac{T_p}{T_r}] - 1 = [\frac{\rho_p}{\rho_r}] - 1 \tag{8.1}$$

Within this expression, the point of difference between the existing theoretical normalization and the experimental normalization is the manner in which the temperature of the products is computed. Observing the difference between the two approaches to computing the heat release ratio, it is clear that experimental data collected within the boundary of the reaction zone of the flame front is in agreement with the theoretical datasets. In this way, the mathematical expression to model flame front oscillatory behavior is also verified from the perspective of thermal parameters. A point of note when examining these results is that these examinations have been limited to the standard conical flame (unlike the study of Re behavior) due to the lack of theoretical models that can be used to verify experimental data for other flame configurations such as the inverted flame or the two-dimensional v-shaped flame. Thus, the combination of the outcomes from the dual parametric study along with the investigation of the effects of flow rate fluctuations shows some important observations that are necessary to address the mitigation of these oscillatory phenomena. These observations are now summarized below:

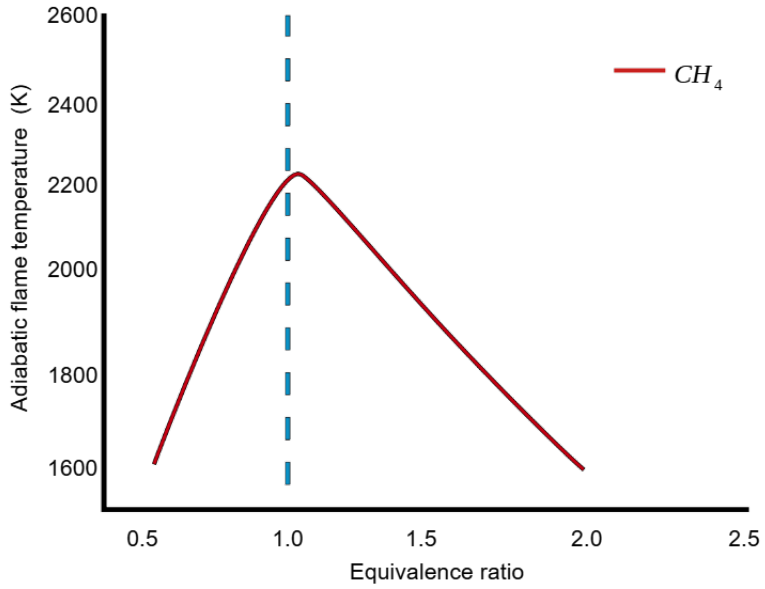

Figure 8.5: Adiabatic flame temperature versus equivalence ratio for a methane-air premixed flame at constant Re [52]. The region of interest for an equivalence ratio of 1.2 lies between 2000-2200 K.

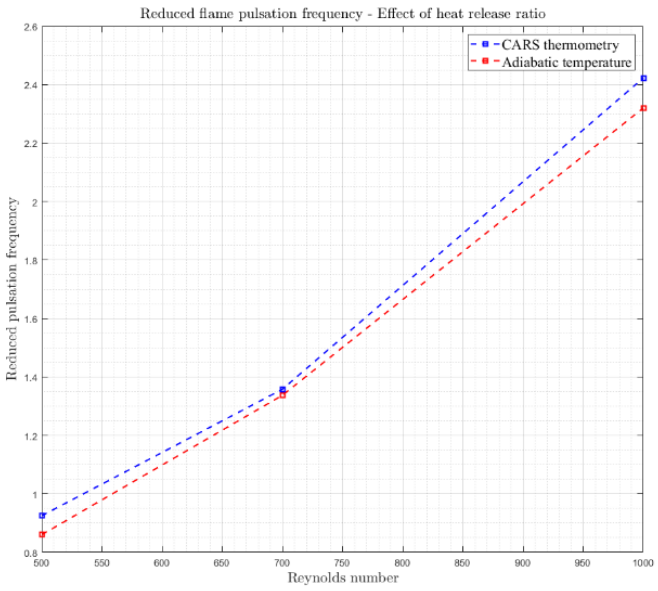

Figure 8.6: Reduced pulsation frequency against Reynolds number – Examining the effect of heat release ratio. The overall trend remains consistent while deviating from the linear trend expected from the investigations by Cheng [48].

- A digitally controlled reactant flow system is capable of a 22-25% uniform reduction in oscillatory frequencies for a laminar premixed flame front across equivalence ratios.
- While minimization of frequencies is possible, complete elimination by addressing the problem of flow rate fluctuations through a system with an order of magnitude higher accuracy was proven to be insufficient.
- The results of investigating flow rate fluctuation as a hypothesis also indicate the possibility of constructing burner designs that can specifically address reactant flow uniformity prior to ignition.
- The effect of buoyancy forces on oscillation frequency is substantially reduced when the inverted flame is compared against the conical flame at varying Reynolds numbers.

- Higher Reynolds number regimes especially show greater suppression of oscillatory frequencies when employing an inverted flame.
- The greater extent of non-linearity present within the trend of an inverted flame with respect to the flow conditions hints at the presence of further variables that are controlling the low-scale oscillatory phenomena.
- While flame inversion may be impractical, the presence of air gradients influencing the flame front when the buoyancy forces are inverted was discovered during these experimental campaigns – this information is of significance when addressing a mitigation solution for the flame front.

9

Efforts towards mitigation

9.1. Modifying conical burners – Mesh placement

As mentioned in the previous chapter, the second half of this study places emphasis on the methods that can be implemented to minimize low-frequency oscillatory instabilities. Having established some significant observations regarding its underlying causes, any burner design that attempts to improve low-scale oscillatory instability of the flame front must possess some basic requirements. The first such requirement is to ensure uniform fuel and oxidizer flow regulation. To this end, the use of the previously evaluated digital flow control system has been considered here as well. Having established this basic requirement, the most significant design is now explained in the following sections. While the stability gain achieved by an inverted conical burner comes with certain trade-offs, a compromise solution without extensive modifications to the burner can be designed. Specifically, the use of a mesh placement at a specified height above the flame front is now proposed as a middle ground in terms of a practical and stable flame-generating solution with regard to low-frequency oscillations. The following schematic representation of such a burner setup for a standard conical flame is now shown in figure 9.1 to demonstrate the simplicity of the modification performed to the basic bunsen burner. As can be observed, the fundamental difference involves a height-adjustable metallic wire mesh placed exactly above the axis of the flame front parallel to the burner lip. At the initial stage, the expectation behind exploring the wire mesh burner arose from the phenomenon referred to as flame anchoring. According to Wan et al [53], the concept of flame anchoring can be explained as the process of stabilizing a flame at a given position. While the methods by which anchoring is performed can vary based on the application involved, the use of a stainless steel wire mesh was expected to stabilize the top extreme of the flame front in the case of this phase of the study.

9.2. Experimental evaluation of mesh burner

In order to evaluate this modified burner design, an experimental campaign was designed using the approach employed during the first phase of the thesis (investigation into oscillatory behavior). To this end, the primary experiment involved fixing the equivalence ratio while varying the Reynolds number over a range of values. It must also be noted here that the height at which the mesh is placed has also been kept constant during the process. Having established the experimental procedure, the diagnostic workflow and reactant flow control scheme can also be finalized. While the existence of high-precision instrumentation such as CARS might be a tempting option solely on the basis of its established workflow, the simplicity of image chemiluminescence led to the latter being employed for the mesh burner. Finally, as stated at the beginning of this chapter, the use of digital flow control via the Bronkhorst EL-FLOW SELECT F-201AV/202AV series of calibrated controllers has been enforced throughout this campaign.

The following plot shown above in figure 9.2 represents the comparative performance of mesh placement at a fixed height of 10mm above the burner outlet. A rich fuel-oxidizer mixture with a range of Reynolds numbers from 500 to 1000 was tested. As is obvious from the difference between the trends for an inverted flame and the meshed flame, the reduction in oscillatory frequency is not as substantial. However, the area of interest is in the change in linearity upon placement of the mesh.

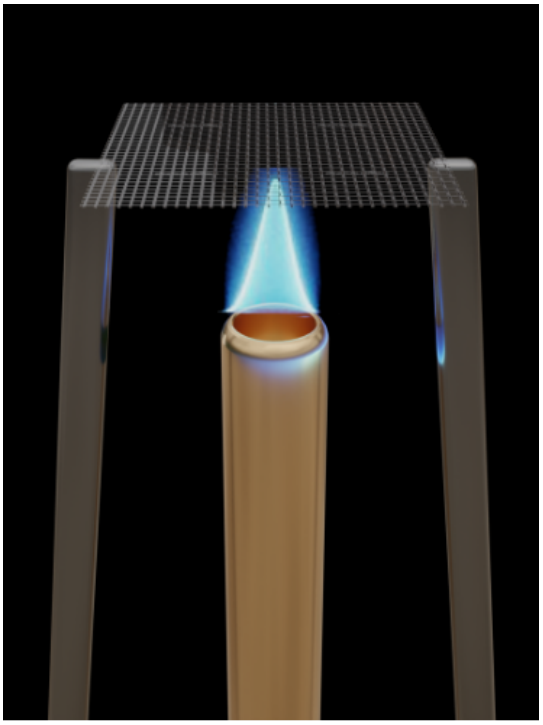

Figure 9.1: Schematic representation of wire mesh placement over the conical flame burner. Note the simple construction and the possibility of varying the position of the mesh with varying flame configurations as needed.

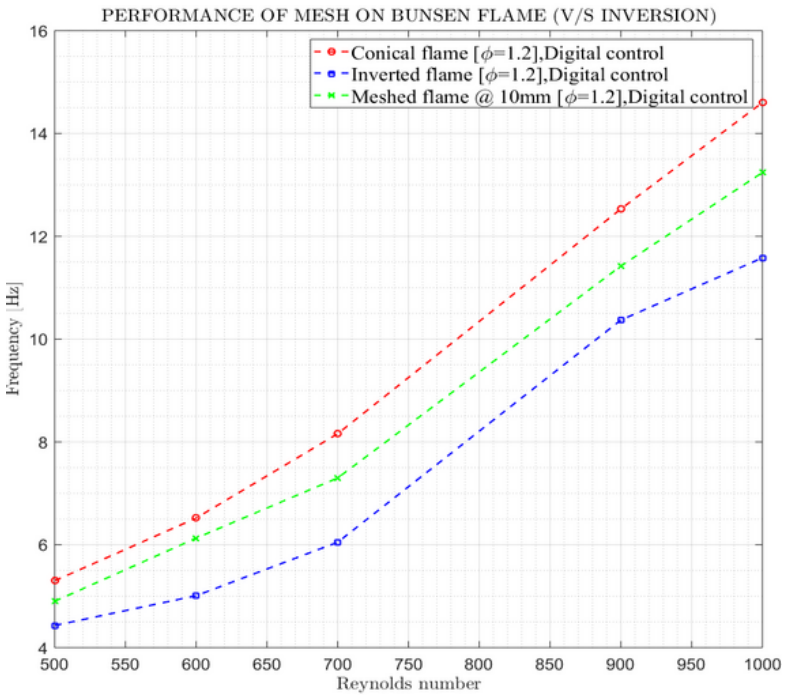

Figure 9.2: Oscillation frequency versus Reynolds number at a constant equivalence ratio for three different flame configurations – Conical, inverted, and mesh burner. The hybrid nature of the mesh burner is visually evident from the adherence to its trend with the conical burner while showing half the effectiveness of the inverted flame in terms of oscillatory instability.

Unlike the inverted flame, the existence of other secondary causes that support the presence of oscillatory behavior is not visible in this burner setup. Specifically, the greater similarity to the standard

conical flame is clearly expected due to only there being minor modifications when placing the mesh atop the conical flame. With a reduction in oscillation frequency ranging from a minimum of 0.5 Hz at lower Reynolds numbers (Re<600) to a maximum of 1.5 Hz for the higher Reynolds number regimes (Re>900). To summarize the performance of this modification, it inherits the suppressive ability to employ an inverted conical burner without the practical difficulties that accompany it such as blow-back and burner tip heating. Thus, this mitigation effort can be considered a hybrid solution to the problem of reducing low-scale oscillatory behavior.

9.3. Effect of varying position of mesh

While the performance evaluation of the mesh placement burner only focused upon a fixed mesh position of 10 mm above the burner lip, some trials prior to this evaluation were also performed at varying positions of 5, 10, and 15 mm above the burner lip. The result of these trials have not been extensively discussed during this phase of the investigation as variations in oscillation frequency with Reynolds number for the three mesh positions have not shown significant differences. The selection of 10 mm over the lower position of 5 mm as the fixed position during the experimental campaign was based on the secondary consideration of avoiding the possibility of damaging the wire mesh due to its interaction with the flame.

10

Conclusion

This investigation into a very specific form of instability for laminar premixed flame fronts was performed in an effort to understand the underlying core causes that are responsible for sustaining such behavior and a practical solution to reduce its presence to a significant extent. Prior to beginning the investigation, observations of the actual phenomenon were made to better visualize the problem at hand. Specifically, this involved reviewing the low-frequency oscillations that were accidentally measured during thermometry analysis of a partially premixed methane-air flame during a CARS spectroscopy study. At the outset, the first step that was taken toward elucidating the core causes of low-frequency flame front oscillations was a literature study of the hypothesis that has been proposed thus far. Among numerous proposals ranging from acoustic resonance [13] to buoyancy-induced oscillations [16] within more contemporary investigations into the phenomenon.

From the dearth of explanations provided both directly and indirectly, some research questions in the form of a dual hypothesis were formulated at the end of the literature study. The first such hypothesis involved the effect of buoyancy forces in the form of varying density gradients. The second hypothesis involved flow rate fluctuations as the driver of low-scale oscillations based on direct first-hand observations made from preceding studies by measuring the reactant flow rates being provided to the premixed burner. Beginning with the primary hypothesis of buoyancy-driven oscillatory behavior, the mathematical model proposed by Cheng et al [14] relating the frequency of oscillation to the fluid and thermal properties of the reactants was employed as the basis for designing the experimental campaign. Among the variables involved, the Reynolds number, heat release ratio, and the flow rate of the reactants were chosen for the parametric study. During the parametric study, digital flow control was also introduced via a dedicated high-accuracy reactant flow metering system employed to control for the possible involvement of flow rate fluctuations. In addition to the standard conical flame that is the centerpiece of this thesis, other flame configurations of interest such as the inverted conical flame as well as the v-shaped flame were also examined. By examining inverted flames, the opposition of the flame-front velocity vectors to the direction of buoyancy forces was expected to eliminate the presence of oscillations in the flame-front. With high-fidelity and low processing time in mind, image chemiluminescence was chosen as the primary diagnostic workflow. By employing an sCMOS imaging device in combination with a 2f telescope optical setup, raw image data were acquired for each flame configuration and parametric variation of interest. While simple in construction, the results produced during the course of investigation have exhibited the excellent performance of this optical setup.

Following acquisition, the luminous reaction zone generated by swan band emissions from the premixed flame is extracted from the image data using custom image processing algorithms. While attempts involving the use of bandpass filters to isolate the spectrum were performed, considerations of the diminished dynamic range of the image data were given precedence over ease of extraction. The processing algorithm employed noise elimination and edge detection techniques such as low pass and high pass filtering which were proven sufficient to extract spatial information from these image sequences. Next, the enhanced imagery was put through pixel tracking algorithms to generate positional data and subsequently frequency spectra for either of the luminous branches of the flame front.

With the diagnostic setup summarized above, the line spread function at full-width half-maximum using a blade edge setup was computed to be 66.5 microns. This measurement also considers the fact that the 2-f telescope system ensures zero magnification as the light passes from the flame to the imaging device. Following the development of the diagnostic pipeline, the same setup was then extended to the experimental campaign for the second hypothesis as well. In terms of the experiments for the second explanation of flow rate fluctuations, a comparative investigation between digital and analog control schemes was performed. Within this campaign, the standard conical flame was tested for fixed flow conditions with varying mixture ratios between the two control schemes. The expectation from this second phase of experiments was a possible reduction in oscillation frequency resulting from greater control over the metering of reactant flow rates. At the end of these experiments, the resulting frequency datasets were analyzed. In the case of the buoyancy hypothesis, the oscillatory trends of standard conical flames were in accordance with the numerical model proposed by Cheng et al [14] when frequency data for various Reynolds numbers were compared with each other. In the case of the inverted conical flame, a substantial reduction in oscillation frequency was observed ranging from 1.4 to 2 Hz.

Despite exhibiting the greatest suppressive ability among all burner configurations that were evaluated to this point, the impracticality and risks of employing an inverted conical burner limited its application. In the case of the thermal parameter (heat release ratio), agreements with the theoretical model via normalization of the pulsation frequency of the flame front were observed for the diagnosed range of reactant flow conditions. In combination with these two parametric studies, the ability of the theoretical model to agree with the experimental observations made was considered sufficiently successful for future considerations of this phenomenon. Based on comparisons made between the standard conical flame and the novel inverted flame, the second phase of this investigation into mitigation efforts was begun. The goal of this section was aimed at a compromise between the ease and simplicity of the standard conical flame against the significant reduction in oscillation frequency observed within the inverted flame. Resulting of these efforts, the simple design of a wire mesh placement burner for a laminar premixed flame was formalized. In order to fully evaluate this design, experiments based on the first phase of investigations in terms of a parametric study were chosen. To this extent, the oscillation frequencies of the flame front at distinct Reynolds numbers were measured. To ensure direct comparisons between the data for the standard conical flame and the inverted, similar flow conditions were chosen. The results of this evaluation showed that a substantial reduction can still be obtained in the range of 0.5 to 1.5 Hz. terms of oscillation frequency but it is not to the same magnitude as the inverted flame. However, the amount of modification necessary to achieve these results proved its greater practicality. Finally, a test of various mesh placement heights was also conducted to search for possible optimum heights prior to finalizing a fixed placement position.

Thus, the big picture arising from the initial phase of investigatory experiments revealed the absence of a single ‘core’ cause. Among these causes, the effects of buoyancy and flow rate fluctuations have been confirmed along with the extent of their influence. Additionally, the experimental outcomes from the inverted burner show the existence of minor contributions that were revealed when buoyancy and flow rate fluctuations were minimized. In addition to the revelations of these experiments, the manner in which they were conducted involving the custom algorithms and acquisition pipelines have also proven their ability to produce useful data from substantially simple setups. In the case of the second phase involving mitigation efforts, the mesh burner was proven to be a good compromise in terms of practicality and suppression of oscillatory behavior. Finally, while there are other possible designs with greater sophistication available, the advantage of the mesh burner in preserving the well-studied characteristics of the standard conical flame while ensuring greater low-scale oscillatory stability as proven by the performance of the inverted flames has been confirmed during the work performed by this investigation.

11

Recommendations for future research

As mentioned earlier, there were some obvious limitations to the manner in which the diagnosis of low-frequency oscillations has been performed. Some recommendations regarding further work that can be done are now outlined below:

1. The effects of flow rate fluctuations while minimized, have still to be completely mitigated. To this end, a comparative analysis between flow controllers with even greater metering control can be performed to observe the extent to which this hypothesis can be extended.
2. While testing the hypothesis involving buoyancy forces as a cause of low-scale oscillations, the existence of minor contributions from unknown causes was revealed by the inverted flame. This suggests the use of such a conical inverted flame as a test burner to perform extended parametric studies with other variables that are part of the numerical model employed during this thesis.
3. During the exploration of practical mitigation efforts based on the results of the parametric studies, the mesh burner was evaluated in terms of its suppressive capability with respect to the flow conditions involved. However, an interesting avenue of research may exist in performing comparisons between various mesh positions as well as mesh densities. The expectation with this suggestion is the possibility of higher mesh densities may lead to a further reduction in oscillation frequency thereby bringing the performance of the mesh burner closer to that of the inverted conical burner.

References

[1] Ahmed Abdulraheem et al. “Measurements and Data Analysis Review of Laminar Burning Velocity and Flame Speed for Biofuel/Air Mixtures Measurements and Data Analysis Review of Laminar Burning Velocity and Flame Speed for Biofuel/Air Mixtures”. In: vol. 1094. May 2021. DOI: 10.1088/1757-899X/1094/1/012029.

[2] A Clarke and G K Hargrave. “Measurements of laminar premixed methane—air flame thickness at ambient conditions”. In: *Proceedings of the Institution of Mechanical Engineers, Part C: Journal of Mechanical Engineering Science* 223.8 (2009), pp. 1969–1973. DOI: 10.1243/09544062JMES1259. eprint: https://doi.org/10.1243/09544062JMES1259. URL: https://doi.org/10.1243/09544062JMES1259.

[3] Francesco Mazza et al. “High-temperature rotational-vibrational O2CO2 coherent Raman spectroscopy with ultrabroadband femtosecond laser excitation generated in-situ”. In: *Combustion and Flame* 237 (2022), p. 111738.

[4] Alexis Bohlin Leonardo Castellanos Dmitrii Kliukin. “On the robustness of space-time CARS imaging thermometry at the study of quasi-laminar premixed flame fronts”. In: 38th International Symposium on Combustion, Adelaide, Jan. 2021.

[5] George H. Markstein. “Experimental and Theoretical Studies of Flame-Front Stability”. In: *Journal of Aeronautical Sciences* 18.3 (1951).

[6] Gerhard Damköhler. “Experimental and Theoretical Studies of Flame-Front Stability”. In: *Journal of Aeronautical Sciences* 46.11 (1947), pp. 601–626.

[7] K.I. Shchelkin. “On combustion in a turbulent flow”. In: *Zhournal Tekhnicheskoi Fiziki* 13 (Dec. 1943), pp. 520–530.

[8] G. H. Markstein. “Cell Structure of Propane Flames Burning in Tubes”. In: *The Journal of Chemical Physics* 17.4 (1949), pp. 428–429. DOI: 10.1063/1.1747278. eprint: https://doi.org/10.1063/1.1747278. URL: https://doi.org/10.1063/1.1747278.

[9] L. CROCCO. “Aspects of Combustion Stability in Liquid Propellant Rocket Motors Part I: Fundamentals. Low Frequency Instability With Monopropellants”. In: *Journal of the American Rocket Society* 21.6 (1951), pp. 163–178. DOI: 10.2514/8.4393. eprint: https://doi.org/10.2514/8.4393. URL: https://doi.org/10.2514/8.4393.

[10] Abbott A. Putnam and William R. Dennis. “Survey of Organ□Pipe Oscillations in Combustion Systems”. In: *The Journal of the Acoustical Society of America* 28.2 (1956), pp. 246–259. DOI: 10.1121/1.1908253. eprint: https://doi.org/10.1121/1.1908253. URL: https://doi.org/10.1121/1.190825.

[11] Shigeo Nakanishi and Charles R King. *Effects of Some Configuration Changes on Afterburner Combustion Performance*. Tech. rep. 1957.

[12] Itsuro Kimura. “Stability of laminar-jet flames”. In: *Symposium (International) on Combustion*. Vol. 10. 1. Elsevier. 1965, pp. 1295–1300.

[13] BD Mugridge. “Combustion driven oscillations”. In: *Journal of Sound and Vibration* 70.3 (1980), pp. 437–452.

[14] Robert K Cheng, Benoit Bédat, and Larry W Kostiuk. “Effects of buoyancy on lean premixed V-flames Part I: laminar and turbulent flame structures”. In: *Combustion and flame* 116.3 (1999), pp. 360–375.

[15] Andres Chaparro, Eric Landry, and Baki M Cetegen. “Transfer function characteristics of bluff-body stabilized, conical V-shaped premixed turbulent propane–air flames”. In: *Combustion and flame* 145.1-2 (2006), pp. 290–299.

[16] AI Krikunova. “Premixed methane-air flame under alternate gravity”. In: *Acta Astronautica* 175 (2020), pp. 627–634.

[17] Joanna Barros et al. “5 kHz single shot hybrid fs/ps-CARS thermometry in an atmospheric flame”. In: *Optics Express* 28.23 (2020), pp. 34656–34664.

[18] V. M. van Essen et al. “Pressure dependence of NO formation in laminar fuel-rich premixed CH4/air flames”. English. In: *Combustion and Flame* 153.3 (May 2008). Cited By (since 1996): 3, pp. 434–441. ISSN: 0010-2180. DOI: 10.1016/j.combustflame.2007.10.006.

[19] Thierry Poinsot and Denis Veynante. *Theoretical and numerical combustion*. RT Edwards, Inc., 2005.

[20] Kanwar Devesh Singh et al. “Computational fluid dynamics modeling of laboratory flames and an industrial flare”. In: *Journal of the Air & Waste Management Association* 64.11 (2014), pp. 1328–1340.

[21] MS Irandoost et al. “Temperature measurement of axisymmetric partially premixed methane/air flame in a co-annular burner using Mach–Zehnder interferometry”. In: *Optics and Lasers in Engineering* 74 (2015), pp. 94–102.

[22] Bader A Alfarraj et al. “The Characterization of Liquefied Petroleum Gas (LPG) Using a Modified Bunsen Burner”. In: *Journal of Combustion* 2022 (2022).

[23] CK Law and CJ Sung. “Structure, aerodynamics, and geometry of premixed flamelets”. In: *Progress in energy and combustion science* 26.4-6 (2000), pp. 459–505.

[24] Moshe Matalon. “Intrinsic flame instabilities in premixed and nonpremixed combustion”. In: *Annu. Rev. Fluid Mech.* 39 (2007), pp. 163–191.

[25] Teodoro Trindade, Artur Ferreira, and Edgar Fernandes. “Characterization of Combustion Chemiluminescence: An Image Processing Approach”. In: *Procedia Technology* 17 (Nov. 2014). DOI: 10.1016/j.protcy.2014.10.228.

[26] Nicolas Blanc. “CCD versus CMOS – has CCD imaging come to an end?” In: (Dec. 2003).

[27] *What is a scientific CMOS camera?* URL: https://andor.oxinst.com/learning/view/article/scmos-technology-what-is-scmos.

[28] Munir El-Desouki et al. “CMOS image sensors for high speed applications”. In: *Sensors* 9.1 (2009), pp. 430–444.

[29] S. Harilal et al. “Optical emission studies of C-2 species in laser-produced plasma from carbon”. In: *Journal of Physics D: Applied Physics* 30 (June 1997). DOI: 10.1088/0022-3727/30/12/003.

[30] Milton Cormier. *Chemiluminescence and bioluminescence*. Springer Science & Business Media, 2013.

[31] Sukesh Roy, James R Gord, and Anil K Patnaik. “Recent advances in coherent anti-Stokes Raman scattering spectroscopy: Fundamental developments and applications in reacting flows”. In: *Progress in Energy and Combustion Science* 36.2 (2010), pp. 280–306.

[32] AB Harvey and JW Nibler. “Coherent anti-Stokes Raman spectroscopy of gases”. In: *Applied Spectroscopy Reviews* 14.1 (1978), pp. 101–143.

[33] Francesco Mazza et al. “Coherent Raman imaging thermometry with in-situ referencing of the impulsive excitation efficiency”. In: *Proceedings of the Combustion Institute* 38.1 (2021), pp. 1895–1904.

[34] Anil K Patnaik et al. “Collisional effects on molecular dynamics in electronic-resonance-enhanced CARS”. In: *Journal of Modern Optics* 55.19-20 (2008), pp. 3263–3272.

[35] Alexis Bohlin, Brian D. Patterson, and Christopher J. Kliewer. “Communication: Simplified two-beam rotational CARS signal generation demonstrated in 1D”. In: *The Journal of Chemical Physics* 138.8 (2013), p. 081102. DOI: 10.1063/1.4793556. eprint: https://doi.org/10.1063/1.4793556. URL: https://doi.org/10.1063/1.4793556.

[36] Zakaniaina Rajaofara et al. “Measurement of the third order nonlinear susceptibility of paratellurite single crystal using multiplex CARS”. In: *AIP Advances* 9.10 (2019), p. 105301. DOI: 10.1063/1.5113478. eprint: https://doi.org/10.1063/1.5113478. URL: https://doi.org/10.1063/1.5113478.

[37] Shigeo Furuno et al. “Nitrogen CARS thermometry for a study of temperature profiles through flame fronts”. In: *Combustion and flame* 54.1-3 (1983), pp. 149–154.

[38] Alan C Eckbreth and Robert J Hall. “CARS thermometry in a sooting flame”. In: *Combustion and Flame* 36 (1979), pp. 87–98.

[39] Ali Hosseinnia. *On the Use of Rotational CARS on Polyatomics and in Time Domain*. 2020.

[40] Stefan Lauxtermann et al. “Comparison of global shutter pixels for CMOS image sensors”. In: *2007 International Image Sensor Workshop*. 2007, p. 8.

[41] *Zyla 5.5 scmos - andor*. URL: https://andor.oxinst.com/products/scmos-camera-series/zyla-5-5-scmos.

[42] TS Anand, Kumaravelu Narasimhan, and P Saravanan. “Performance evaluation of image fusion using the multi-wavelet and curvelet transforms”. In: *IEEE-International Conference On Advances In Engineering, Science And Management (ICAESM-2012)*. IEEE. 2012, pp. 121–129.

[43] *Edge Detection*. 2022. URL: https://www.mathworks.com/help/images/edge-detection.html.

[44] Darren Tanner et al. “On high-pass filter artifacts (they’re real) and baseline correction (it’s a good idea) in ERP/ERMF analysis”. In: *Journal of Neuroscience Methods* 266 (Jan. 2016). DOI: 10.1016/j.jneumeth.2016.01.002.

[45] Steven Harvey. “Interactive computer methods for morphometric and kinematic measurement of images of the spine.” PhD thesis. Aug. 1999.

[46] *Fast Fourier Transform*. 2022. URL: https://www.mathworks.com/help/matlab/ref/fft.html.

[47] Guy Meynants et al. “Limitations to the frame rate of high speed image sensors”. In: *Proc. Int. Image Sensor Workshop*. 2009, pp. 153–156.

[48] LW Kostiuk and RK Cheng. “The coupling of conical wrinkled laminar flames with gravity”. In: *Combustion and Flame* 103.1-2 (1995), pp. 27–40.

[49] Qianpeng ZHAO et al. “Lean blowout characteristics of spray flame in a multi-swirl staged combustor under different fuel decreasing rates”. In: *Chinese Journal of Aeronautics* 35.12 (2022), pp. 130–143. ISSN: 1000-9361. DOI: https://doi.org/10.1016/j.cja.2022.06.008. URL: https://www.sciencedirect.com/science/article/pii/S1000936122001169.

[50] B Ashok. *NOx Emission Control Technologies in Stationary and Automotive Internal Combustion Engines: Approaches Toward NOx Free Automobiles*. Elsevier, 2021.

[51] András Urbán et al. “Application of big data analysis technique on high-velocity airblast atomization: Searching for optimum probability density function”. In: *Fuel* 273 (2020), p. 117792.

[52] Steven Jansto. “The Integration of Process and Product Metallurgy in Niobium Bearing Steels”. In: *Metals* 8 (Aug. 2018), p. 671. DOI: 10.3390/met8090671.

[53] Jianlong Wan, Cheng Shang, and Haibo Zhao. “Anchoring mechanisms of methane/air premixed flame in a mesoscale diverging combustor with cylindrical flame holder”. In: *Fuel* 232 (Nov. 2018). DOI: 10.1016/j.fuel.2018.06.027.

A

Equipment List

In this Appendix, a list is provided of the used equipment. The list consists of the optical elements, control system and camera setup. It must be noted here that the light sources (premixed burner) and support stands for the optical elements have not been listed.

Table A.1: Components utilized during experimental campaign

Name	Manufacturer	Item code	Description
Primary camera	Oxford instruments	ZYLA-5.5-USB3	Pixel size = 6.5 microns
Beam profiling camera	DataRay	S-WCD-LCM	Pixel size = 5.5 microns
Fuel flow controller	Bronkhorst	EL-FLOW Select F-201AV	min 0.4-20 LPM
Oxidizer flow controller	Bronkhorst	EL-FLOW Select F-202AV	max 5-250 LPM
Optical delay stage (CARS)	Thorlabs	ODL100(/M)	sub-10 fs resolution
Transmission gratings	Ibsen Photonics	PCG-3039.5/450-810	3040 lines/mm
f100 plano-convex lens	Thorlabs	LA1050-A	
f300 plano-convex cylindrical lens	Thorlabs	LA1256-A	